AGU PUBLICATIONS

JGR

Journal of Geophysical Research: Oceans

RESEARCH ARTICLE
10.1002/2017JC012756

Special Section:
Oceanic Responses and Feedbacks to Tropical Cyclones

# Rapid shelf-wide cooling response of a stratified coastal ocean to hurricanes

Greg Seroka[1,2], Travis Miles[1], Yi Xu[3], Josh Kohut[1], Oscar Schofield[1], and Scott Glenn[1]

[1]Center for Ocean Observing Leadership, Department of Marine and Coastal Sciences, School of Environmental and Biological Sciences, Rutgers University, New Brunswick, New Jersey, USA, [2]I.M. Systems Group, Inc., and Ocean Prediction Center, NOAA/NWS/NCEP, College Park, Maryland, USA, [3]State Key Laboratory of Estuarine and Coastal Research, East China Normal University, Shanghai, China

**Key Points:**
- Observations, models reveal similar processes governing stratified coastal ocean cooling response to Hurricane Irene, Tropical Storm Barry
- Robust shear-induced mixing produced rapid ahead-of-eye-center cooling in TCs on opposite ends of track and seasonal stratification envelope
- Coupled TC models capable of predicting processes leading to rapid cooling of stratified coastal oceans critical for populated coastlines

**Correspondence to:**
G. Seroka,
gregory.seroka@noaa.gov

**Citation:**
Seroka, G., T. Miles, Y. Xu, J. Kohut, O. Schofield, and S. Glenn (2017), Rapid shelf-wide cooling response of a stratified coastal ocean to hurricanes, *J. Geophys. Res. Oceans*, *122*, 4845–4867, doi:10.1002/2017JC012756.

Received 30 JAN 2017
Accepted 12 MAY 2017
Accepted article online 20 MAY 2017
Published online 15 JUN 2017



**Abstract** Large uncertainty in the predicted intensity of tropical cyclones (TCs) persists compared to the steadily improving skill in the predicted TC tracks. This intensity uncertainty has its most significant implications in the coastal zone, where TC impacts to populated shorelines are greatest. Recent studies have demonstrated that rapid ahead-of-eye-center cooling of a stratified coastal ocean can have a significant impact on hurricane intensity forecasts. Using observation-validated, high-resolution ocean modeling, the stratified coastal ocean cooling processes observed in two U.S. Mid-Atlantic hurricanes were investigated: Hurricane Irene (2011)—with an inshore Mid-Atlantic Bight (MAB) track during the late summer stratified coastal ocean season—and Tropical Storm Barry (2007)—with an offshore track during early summer. For both storms, the critical ahead-of-eye-center depth-averaged force balance across the entire MAB shelf included an onshore wind stress balanced by an offshore pressure gradient. This resulted in onshore surface currents opposing offshore bottom currents that enhanced surface to bottom current shear and turbulent mixing across the thermocline, resulting in the rapid cooling of the surface layer ahead-of-eye-center. Because the same baroclinic and mixing processes occurred for two storms on opposite ends of the track and seasonal stratification envelope, the response appears robust. It will be critical to forecast these processes and their implications for a wide range of future storms using realistic 3-D coupled atmosphere-ocean models to lower the uncertainty in predictions of TC intensities and impacts and enable coastal populations to better respond to increasing rapid intensification threats in an era of rising sea levels.

## 1. Introduction

Although substantial progress in the prediction of tropical cyclone (TC) tracks has been realized globally over the past few decades, TC intensity prediction skill has remained comparatively flat across all TC ocean basins [*DeMaria et al*., 2014; *Sopko and Falvey*, 2014; *Cangialosi and Franklin*, 2016]. This intensity gap can be traced to high-resolution requirements for TC models, poor understanding and modeling of the atmospheric boundary layer, difficulty for many existing assimilation techniques to ingest observations of small but intense features, and—most importantly for this study—challenges in modeling the upper ocean response to TCs [*Emanuel*, 2017, and references therein]. Large uncertainty in predicting the strength of TCs thus remains, which has its most significant implications for landfalling TCs where impacts to life and property—via storm surge, wind damage, and inland flooding—are greatest. These storms must first traverse the shallow, coastal ocean before making landfall. The number of studies in the literature investigating shallow, coastal ocean TC responses, indeed, pales in comparison to the number examining deep, open ocean TC responses [*Seroka et al*., 2016]. Further, the differences between the deep, open ocean processes and the coastal processes are stark due to the influence of the bottom boundary layer and coastal wall in shallow water [*Glenn et al*., 2016; *Seroka et al*., 2016]. It is critical to close this gap, with the goal of improving the simulation of coastal ocean physics in coupled TC intensity models [e.g., *Zambon et al*., 2014; *Warner et al*., 2017].

In the summer hurricane season, the shallow Mid-Atlantic Bight (MAB) off the U.S. East Coast is one of the most seasonally stratified regions in the world [*Schofield et al*., 2008], characterized by a sun-heated warm (>25°C) and thin (10 m or less) surface layer and a cold (<10°C) bottom layer termed the "Cold Pool"

[*Houghton et al*., 1982]. When Hurricane Irene traversed the highly stratified, shallow MAB waters in August 2011 before making landfall in New Jersey, rapid surface cooling caused by mixing processes resulting from the two-layer baroclinic circulation in the MAB were observed by an underwater glider and several National Data Buoy Center (NDBC) buoys; these intense mixing processes and the surface cooling (up to 11°C) response in the MAB are described in detail in *Glenn et al*. [2016]. Because the magnitude of the cooling was so significant, it led to a reversal in the direction of air-sea latent and sensible heat fluxes—from the ocean providing heat to the storm when using a fixed prestorm warm sea surface temperature (SST) bottom boundary condition to the ocean acting as a heat sink when using the fixed poststorm cold SST condition [*Seroka et al*., 2016].

This cooling was also found to primarily occur ahead of Irene's eye center—critical for direct impact on storm intensity—as the storm traversed northeastward along the MAB coastline. The cascade of processes responsible were strong ahead-of-eye-center onshore winds and surface currents, coastal setup with water piling up along the coast, offshore bottom currents in response to the resulting offshore pressure gradient, and larger shear-driven turbulence, mixing, and entrainment of cold bottom water to the surface due to directly opposing onshore surface and offshore bottom currents.

The ahead-of-eye-center cooling signal that resulted from these baroclinic coastal ocean mixing processes was found to be present in the 10 additional storms since 1985 that traversed northeastward across the MAB in the summer stratified season, and also in Super Typhoon Muifa (2011) in the similarly highly stratified Yellow Sea between eastern China and Korea. Further, this ahead-of-eye-center cooling was found to have a large impact on Hurricane Irene's intensity, larger than any other Weather Research and Forecasting (WRF) parameter tested [*Seroka et al*., 2016].

Many questions remain. First, it is not known to what extent the ahead-of-eye-center cooling impacted the intensities of the other 10 MAB storms and Typhoon Muifa. Extensive sensitivity studies like the one performed by *Seroka et al*. [2016] would need to be conducted for each storm to investigate these intensity impacts.

Second, it is not known if the same or different cooling processes occurred in the other 10 MAB storms and in Typhoon Muifa. To improve understanding of TC coastal ocean response, the dominant momentum balances that occurred in these storms as well as mixing versus advective processes that led to the ahead-of-eye-center cooling signals should be investigated in detail. It is also critical to understand the spatial—cross-shelf and along-shelf, shallow and deep water—variability of the cooling processes, for a wider range of storms including Irene. Previous studies focused on these processes at the underwater glider location and not elsewhere on the MAB continental shelf [i.e., *Glenn et al*., 2016]. These research gaps will guide this paper's work.

Standard operational model annual performance metrics are based on the mean across all storms simulated during one or several hurricane seasons [e.g., *Kim et al*., 2014; *Tallapragada et al*., 2014; *Cangialosi and Franklin*, 2016]. While this method is effective in testing overall performance of a model, it tends to wash out any unique storm characteristics in both the atmosphere and the ocean. The full range of storm characteristics represents the full range of storm air-sea feedbacks that coupled models should capture and resolve. Therefore, it is critical to not only improve models incrementally based on the mean in an operational environment [e.g., *Kim et al*., 2014; *Tallapragada et al*., 2014; *Cangialosi and Franklin*, 2016] but also to investigate individual case studies and processes that models may or may not be correctly resolving [e.g., *D'Asaro et al*., 2007; *Lin et al*., 2009; *Jaimes and Shay*, 2015; *Glenn et al*., 2016; *Seroka et al*., 2016].

In order to better understand the baroclinic ocean response for different storms, further investigation was performed on Irene and Tropical Storm Barry (2007), 1 of the other 10 MAB storms listed in *Glenn et al*. [2016]. A map of National Hurricane Center (NHC) best tracks for Irene and Barry show both storms traversing northeastward over the MAB, with Irene traveling 600 km from eastern North Carolina (NC) to New York City in 19 h in late August 2011 (∼32 km/h translation speed), and Barry traveling 700 km from eastern NC to just south of Montauk Point, NY in 18 h in early June 2007 (∼39 km/h translation speed, Figure 1, left). Typical translation speeds at MAB latitudes are 29–36 km/h [*Mei et al*., 2012]. Intensity time series show Irene weakening throughout its MAB crossing using both wind and pressure intensity metrics and show Barry weakening—at a lesser rate than Irene—over its last 12 h across the MAB using both metrics (Figure 1, right). Both storms had a radius of maximum wind (RMW) reported in the Automated Tropical Cyclone Forecast (ATCF) [*Sampson and Schrader*, 2000] system database of ∼74 km 30 h prior to storm presence

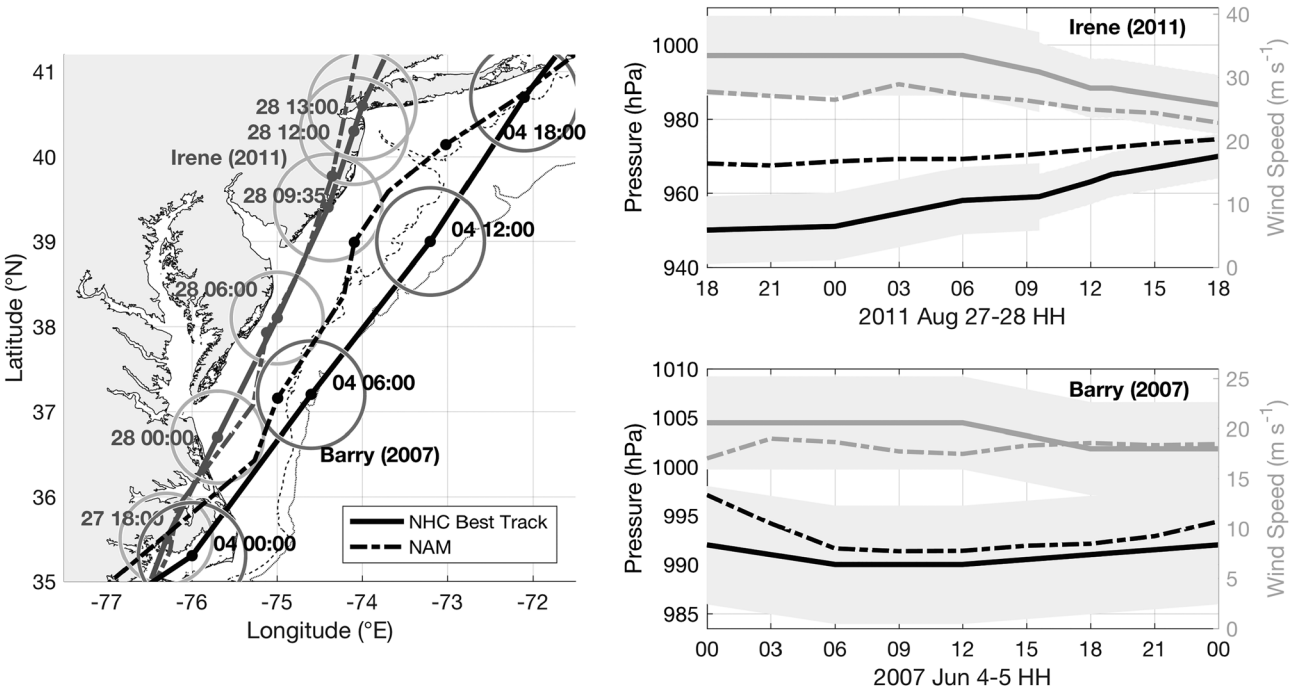


**Figure 1.** Irene and Barry. NHC best track spatial map (left) for Irene (gray solid line) and Barry (black solid line), with position uncertainty circles plotted at each NHC best track position for each storm. NAM in dash-dotted line for Irene (gray) and Barry (black). 50 and 200 m isobaths are in dotted contours. Date and time are in format 2011 MM HH:MM for Irene and 2007 MM HH:MM for Barry. NHC best track intensity time series for Irene (top right) and Barry (bottom right), with minimum central pressure (hPa) in solid black line and maximum sustained 10 m wind speeds (m $s^{-1}$) in solid gray line and intensity uncertainty in shaded gray. NAM in black dash-dotted lines for minimum central pressure and gray dash-dotted lines for maximum winds. NHC best track position and intensity uncertainties are from [*Torn and Snyder*, 2012] and depend on the intensity of the TC. All times are in UTC.

over eastern NC, with Irene's RMW increasing to 185 km 36 h later when the storm was over the MAB. For context, the average RMW for hurricanes making landfall in the U.S. from 1893 to 1979 was 47 km [*Hsu and Yan*, 1998].

For both of these storms, Rutgers University underwater gliders were deployed on the MAB continental shelf. Irene had a more inshore track northward through the MAB and Barry tracked farther offshore along the shelf break (Figure 1). Irene occurred in late August toward the end of the MAB summer stratified season, while Barry occurred in early June, during the beginning of the summer stratified season. However, the intent is not to perform direct comparisons between the two storms, as this would introduce several uncontrollable variables and not be a fully controlled experiment. Rather, the objective is to better understand the conditions in both the atmosphere and ocean that may lead to the baroclinic coastal ocean cooling processes, ahead-of-eye-center cooling, and impact on storm intensities for two extremes in the storm track—one nearshore and one well offshore—and two extremes in summer stratification—one near the end and one near the beginning of the season. This paper will investigate the details of and variability in the dominant baroclinic coastal ocean processes—in both the cross-shelf and along-shelf directions—for both Irene and Barry. By studying the spatiotemporal variability in these baroclinic coastal ocean cooling TC processes, the aim will be to improve the modeling of the full range of stratified coastal ocean TC responses.

## 2. Data and Methods

### 2.1. High Frequency (HF) Radar

Hourly surface ocean current data, 1 h center-averaged, from a network of CODAR Ocean Sensors SeaSonde HF Radar stations [*Roarty et al.*, 2010] along the MAB coast were used in this paper. Surface current map data have a nominal 6 km spatial resolution (Figure 1).

### 2.2. Gliders

Teledyne-Webb Research (TWR) Slocum gliders, autonomous underwater vehicles (AUVs), were used in this paper [*Schofield et al.*, 2007; *Glenn et al.*, 2008, 2016; *Ruiz et al.*, 2012; *Miles et al.*, 2013, 2015]. Rutgers

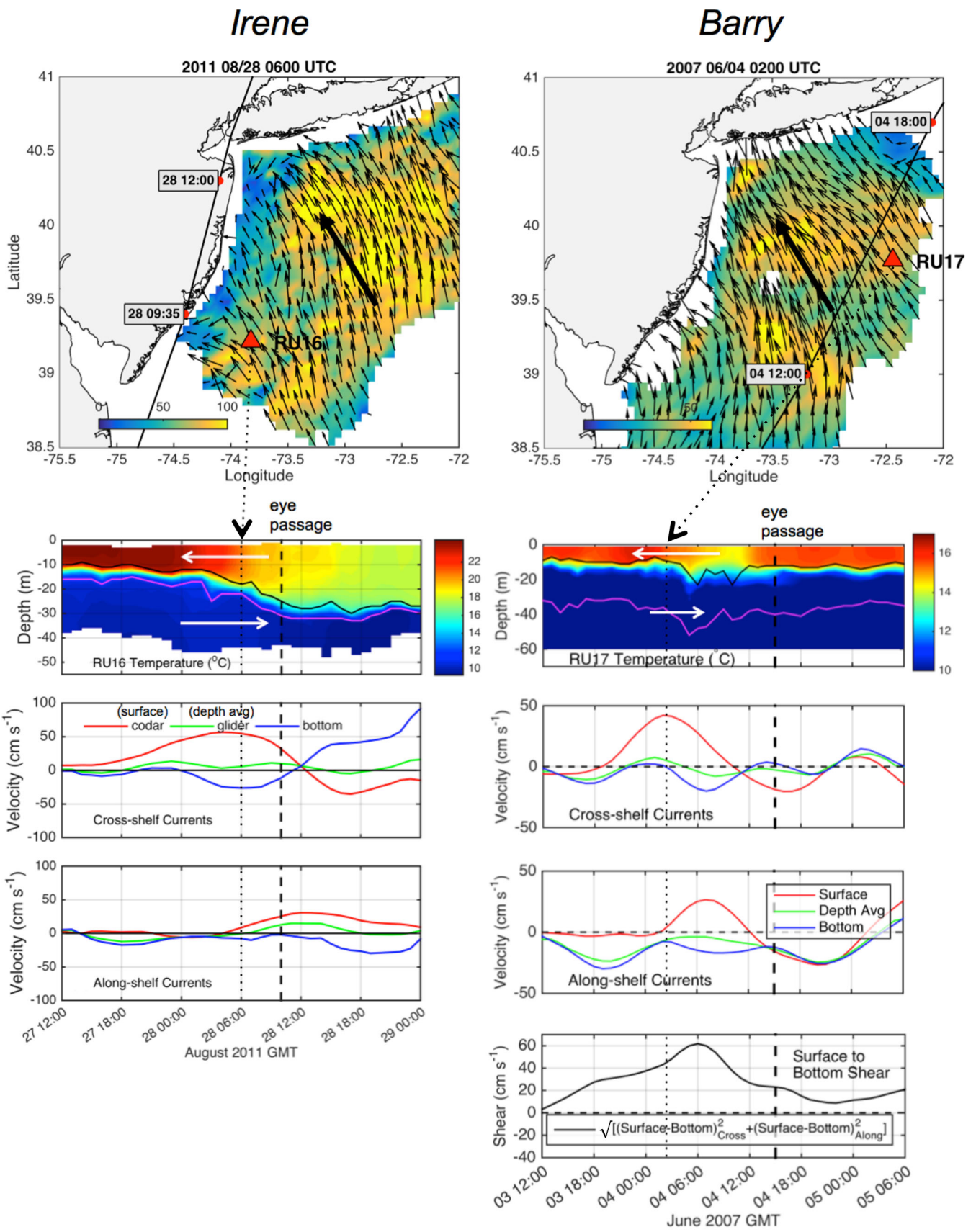
Irene
Barry
2011 08/28 0600 UTC
2007 06/04 0200 UTC
28 12:00
28 09:35
04 18:00
04 12:00
RU16
RU17
Latitude
Longitude
eye passage
RU16 Temperature (°C)
RU17 Temperature (°C)
Depth (m)
(surface)
(depth avg)
codar
glider
bottom
Cross-shelf Currents
Along-shelf Currents
Velocity (cm s-1)
Surface
Depth Avg
Bottom
Surface to Bottom Shear
Shear (cm s-1)
√[(Surface-Bottom)2Cross+(Surface-Bottom)2Along]
27 12:00
27 18:00
28 00:00
28 06:00
28 12:00
28 18:00
29 00:00
August 2011 GMT
03 12:00
03 18:00
04 00:00
04 06:00
04 12:00
04 18:00
05 00:00
05 06:00
June 2007 GMT

**Figure 2.**

University Gliders RU16 (Irene) and RU17 (Barry) data were analyzed. Both gliders were equipped with a Seabird unpumped conductivity, temperature, and depth (CTD) sensor.

Depth and time-averaged velocity calculations were performed using a dead-reckoning technique, a method typically used for underwater gliders [*Sherman et al*., 2001; *Davis et al*., 2002; *Schofield et al*., 2007]. To estimate bottom layer currents at the glider location, a combination of dead-reckoned depth-averaged glider currents and HF radar surface currents is used (Figure 2). This method assumes that the HF radar surface currents are representative of the currents in the surface mixed layer above the thermocline. See *Glenn et al*. [2016] for detailed methods and equations used to calculate bottom layer currents.

### 2.3. Bathymetry

U.S. Coastal Relief Model data from the NOAA National Centers for Environmental Information were used for water depth and coastlines throughout this paper [*NOAA National Centers for Environmental Prediction*, 2016].

### 2.4. Satellite SST

Advanced Very High Resolution Radiometer (AVHRR) data were used for ocean model SST verification. Techniques empirically derived for the MAB to remove bright cloud covered pixels and retain darker ocean pixels were used to decloud AVHRR data but preserve the rapid TC cooling signal, following *Glenn et al*. [2016].

### 2.5. Regional Ocean Modeling System (ROMS): ESPreSSO

Ocean model simulations were conducted using ROMS [*Haidvogel et al*., 2008], a free-surface, sigma coordinate, primitive equation ocean model (code available at http://www.myroms.org). ROMS has been used for a wide variety of coastal applications. Specifically, the ESPreSSO (Experimental System for Predicting Shelf and Slope Optics) model [*Wilkin and Hunter*, 2013], covering the MAB from Cape Cod to south of Cape Hatteras, and from the inland bays to beyond the shelf break, was used for simulations. In an assessment of skill of real-time ocean models over the MAB continental shelf for 2010–2011, ESPreSSO performed well as compared to global models and other regional models, indicating its usefulness for simulating coastal ocean circulations across a wide range of conditions, including Hurricane Irene which also occurred in 2011 [*Wilkin and Hunter*, 2013].

The ESPreSSO grid has a horizontal resolution of 5 km and 36 vertical levels in a terrain-following *s*-coordinate system. Initial conditions here were developed from an ESPreSSO grid ROMS reanalysis with strong constrained four-dimensional variational (4D-Var) data assimilation, including assimilation of sea surface height, SST, HF radar surface currents, and in situ temperature and salinity observations. For atmospheric forcing, North American Mesoscale (NAM) 12 km 3 hourly forecast data from its daily 00Z cycles were used. Only short-term forecast hours f03–f27 were used to limit any longer-term forecast error, with the f00 analysis skipped to allow for model spin-up. NAM surface air temperature, pressure, relative humidity, 10 m vector winds, precipitation, downward longwave radiation, and net shortwave radiation were used to specify the surface momentum and buoyancy fluxes based on the COARE bulk formulae [*Fairall et al*., 2003].

The NAM track map and intensity time series as assembled here for both Irene and Barry are compared to the NHC best track analyses (Figure 1). NHC best track uncertainty estimates depend on the intensity of the TC, with the uncertainty increasing as the intensity decreases [*Torn and Snyder*, 2012]. For both storms, the NAM tracks are all well within or just outside the best track uncertainties, and the NAM maximum wind intensities are within or at the best track uncertainties (Figure 1). For Barry, the minimum central pressure intensities are well within the uncertainties, and for Irene, they are at or just outside the uncertainties. The wind rather than central pressure intensities are most relevant for this study, as the winds provide the momentum fluxes forcing the TC ocean response. Overall, the NAM tracks properly represent the typical MAB track envelope, with Irene propagating along the inner shelf and Barry along the mid to outer shelf.

**Figure 2.** Irene and Barry. HF radar surface ocean current 1 h center-averaged maps for Irene and Barry before eye passage by RU16 (Irene, top left) and RU17 (Barry, top right). NHC best track in black, with large black arrow indicating general direction of surface currents. Location of RU16 and RU17 shown with red triangles. Time series at glider locations of temperature with thermocline depth in black contour, transition layer depth (see *Glenn et al*. [2016] for definitions) in magenta contour, and large white arrows indicating general direction of layer currents (second row from top); cross-shelf currents (third row from top); along-shelf currents (fourth row); and surface to bottom shear for Barry (bottom right). Currents and shear are smoothed using the MATLAB "smooth" function using a span of 8.

Boundary conditions were daily two-dimensional surface elevation and three-dimensional velocity, temperature, and salinity fields from the Hybrid Coordinate Ocean Model (HYCOM) Navy Coupled Ocean Data Assimilation (NCODA) forecast system. River inflows were from the seven largest rivers, using daily average U.S.G.S. discharge data. Tidal boundary conditions were from the ADvanced CIRCulation (ADCIRC) tidal model. Finally, vertical turbulence diffusivity was determined using the general length-scale method k-kl type vertical mixing scheme [*Umlauf and Burchard*, 2003; *Warner et al*., 2005].

For Barry, the ROMS ESPreSSO simulation was initialized at 1200 UTC on 29 May 2007 and ended at 1200 UTC on 8 June 2007, with storm eye passage by glider RU17 at 1700 UTC on 4 June 2007, just over 5 days into the simulation to allow for model spin-up. For Irene, the ROMS ESPreSSO simulation was initialized at 1200 UTC on 24 August 2011 and ended at 0000 UTC on 3 September 2011, with storm eye passage by glider RU16 at 1200 UTC on 28 August 2011, exactly 4 days into the simulation.

The depth-averaged momentum balance terms were direct output from the ROMS simulations, and the equations are as follows:

$$\underbrace{\frac{\partial u}{\partial t}}_{\text{acceleration}} = -\underbrace{\frac{\partial (uu)}{\partial x} - \frac{\partial (vu)}{\partial y}}_{\text{horizontal advection}} - \underbrace{\frac{1}{\rho_0}\frac{\partial P}{\partial x}}_{\text{pressure gradient}} + \left( \underbrace{\frac{\tau_s^x}{h\rho_0}}_{\text{surface stress}} - \underbrace{\frac{\tau_b^x}{h\rho_0}}_{\text{bottom stress}} \right) + \underbrace{fv}_{\text{Coriolis}}, \tag{1}$$

$$\underbrace{\frac{\partial v}{\partial t}}_{\text{acceleration}} = -\underbrace{\frac{\partial (uv)}{\partial x} - \frac{\partial (vv)}{\partial y}}_{\text{horizontal advection}} - \underbrace{\frac{1}{\rho_0}\frac{\partial P}{\partial y}}_{\text{pressure gradient}} + \left( \underbrace{\frac{\tau_s^y}{h\rho_0}}_{\text{surface stress}} - \underbrace{\frac{\tau_b^y}{h\rho_0}}_{\text{bottom stress}} \right) - \underbrace{fu}_{\text{Coriolis}}, \tag{2}$$

where $u$ and $v$ are the along-shelf and cross-shelf components of depth-averaged velocity, respectively, $t$ is time, $P$ is depth-averaged pressure, $\rho_o$ is a reference density, $\tau_s$ and $\tau_b$ are surface (wind) and bottom stresses, $h$ is water column depth, and $f$ is the latitude-dependent Coriolis frequency. Horizontal diffusion was small and neglected here.

The temperature rate equation terms to diagnose advection versus mixing were also direct output from ROMS. The equation is as follows:

$$\frac{\partial T}{\partial t} = -\frac{\partial (uT)}{\partial x} - \frac{\partial (vT)}{\partial y} - \frac{\partial (wT)}{\partial z} + \frac{\partial A_{kt}\frac{\partial T}{\partial z}}{\partial z} + D_T + F_T, \tag{3}$$

with the following surface and bottom boundary conditions, respectively:

$$\left( A_{kt}\frac{\partial T}{\partial z} \right)_{z=0} = \frac{Q_{net}}{\rho_0 C_p}, \tag{4}$$

$$\left( A_{kt}\frac{\partial T}{\partial z} \right)_{z=0} = 0. \tag{5}$$

Here $T$ is the temperature, $t$ is time, $u$, $v$, and $w$ are the along-shelf, cross-shelf, and vertical components of velocity. $A_{kt}$ is the vertical diffusivity coefficient, $D_T$ is the horizontal diffusion term, and $F_T$ is friction. $Q_{net}$ is the surface net heat flux, $\rho_0 = 1025$ kg m$^{-3}$ is a reference density, $C_p = 3985$ J (kg °C)$^{-1}$ is the specific heat capacity of seawater, and $h$ is the water depth. Horizontal diffusion again was small and neglected here.

## 3. Results

### 3.1. Observations

*Glenn et al*. [2016] used HF radar and glider RU16 data to determine surface, depth-averaged, and bottom currents at the glider location during Irene. Part of the time series is repeated here in Figure 2 for ease of comparison to a similar analysis for Barry. At 0600 UTC on 28 August 2011, less than 4 h before Irene's NJ landfall and eye passage by glider RU16, surface ocean currents were directed onshore and upshelf, aligning close to the onshore winds ahead of Irene's eye (Figure 2, top left). Current magnitudes at this time approached 1 m s$^{-1}$. At 0200 UTC on 4 June 2007, a full 15 h before Barry's eye passage by glider RU17, surface ocean currents were in a very similar direction, onshore and upshelf.

Time series of temperature profiles at the glider locations below the surface current maps indicate initially very strong stratification and an eventual breakdown in stratification upon storm forcing. For Irene in late August, surface mixed-layer temperatures approached 25°C to ~10–15 m depth, and bottom MAB Cold Pool temperatures were less than 10°C. For Barry in early June, surface mixed-layer temperatures down to ~10–15 m depth were approaching 16°C with bottom MAB Cold Pool temperatures again less than 10°C, approaching 5°C. For Irene, the thermocline (black contour) deepened to ~30 m depth and surface mixed-layer temperatures cooled to ~17°C, with much (~5°C, or ~75%) of the cooling occurring ahead-of-eye-center. For Barry, the thermocline (black contour) deepened briefly to 25 m depth and surface mixed-layer temperatures cooled to nearly 14°C, with 100% of the cooling at RU17 occurring ahead-of-eye-center.

Cross-shelf and along-shelf surface (red), depth-averaged (green), and bottom (blue) current time series are depicted in the two figures below the temperature time series in Figure 2. For Irene, currents in Earth coordinates are rotated 31° clockwise from north to attain cross-shelf and along-shelf components. For Barry, currents in Earth coordinates are rotated 50° clockwise from north to attain cross-shelf and along-shelf components. For both Irene and Barry, red surface currents peaked onshore ahead-of-eye-center, and blue bottom currents peaked offshore at the same time yet with a bit of a lag in setup. For Irene, along-shelf currents were very small ahead-of-eye-center, but for Barry, along-shelf surface currents to the northeast peaked ahead-of-eye-center and bottom currents peaked just before. For both storms, observations indicate a two-layer circulation, with cross-shelf surface currents onshore and cross-shelf bottom currents offshore, enhancing the shear and resultant mixing and cooling. For Barry, a similar surface to bottom shear profile occurred in the along-shelf direction. Figure 2 (bottom right) shows a calculation of surface to bottom shear, combining both the along-shelf and cross-shelf components for Barry due to the large observed along-shelf component. Maximum shear occurred at the same time as maximum surface cooling and thermocline deepening, and well before eye passage.

### 3.2. Modeling

In order to investigate the details of the baroclinic processes and mixing that occurred in Irene and Barry, including momentum balance analysis and the temperature diagnostic equation for mixing versus advection comparisons, ROMS ESPreSSO simulations were performed as described in section 2.5 above.

#### 3.2.1. ROMS Simulation Validation: Hurricane Irene (2011)

A prestorm map of SST over the MAB from AVHRR at 0742 UTC on 24 August 2011 (Figure 3, top left) shows coastal upwelling along the NJ, DE, and MD coastlines, with a warm tongue of SST through the southern MAB and extending offshore of the 50 m isobath and into the northern MAB north of the Hudson Canyon. The ROMS ESPreSSO rerun SST ~4 h later (Figure 3, top right) shows very good agreement with AVHRR, capturing the coastal upwelling, warm tongue, Gulf Stream, and colder waters south of Rhode Island and Nantucket.

A poststorm map of SST over the MAB from AVHRR at 0828 UTC on 29 August 2011 (Figure 3, middle left) shows a much different story, with cold <18°C SST from the mouth of the Hudson Canyon and northward, and a corridor of colder water at the 50 m isobath and offshore in the southern MAB. The ROMS ESPreSSO rerun SST (Figure 3, middle right) again shows very good agreement with AVHRR, with perhaps the only minor issue being not as cold water at the mouth of the Delaware Bay and in the southern MAB.

A difference map of poststorm minus prestorm AVHRR SST (Figure 3, bottom left) shows maximum cooling (approaching 11°C) at the mouth of the Hudson Canyon and across the MAB, with less cooling in the shallow regions of the shelf and offshore in the deep water. Again, ROMS (Figure 3, bottom right) agrees very well with the AVHRR cooling map, capturing the maximum in cooling at the Hudson Canyon mouth.

Finally, RU16 glider temperature profile time series (Figure 4, left) shows the same deepening of the thermocline and cooling of the surface layer as shown in Figure 2. ROMS (Figure 4, right) taken at the closest grid cell to the average position of RU16 during the storm period shows an initial thermocline ~10–15 m too deep but with correct surface mixed layer and bottom layer temperatures. Although the simulated

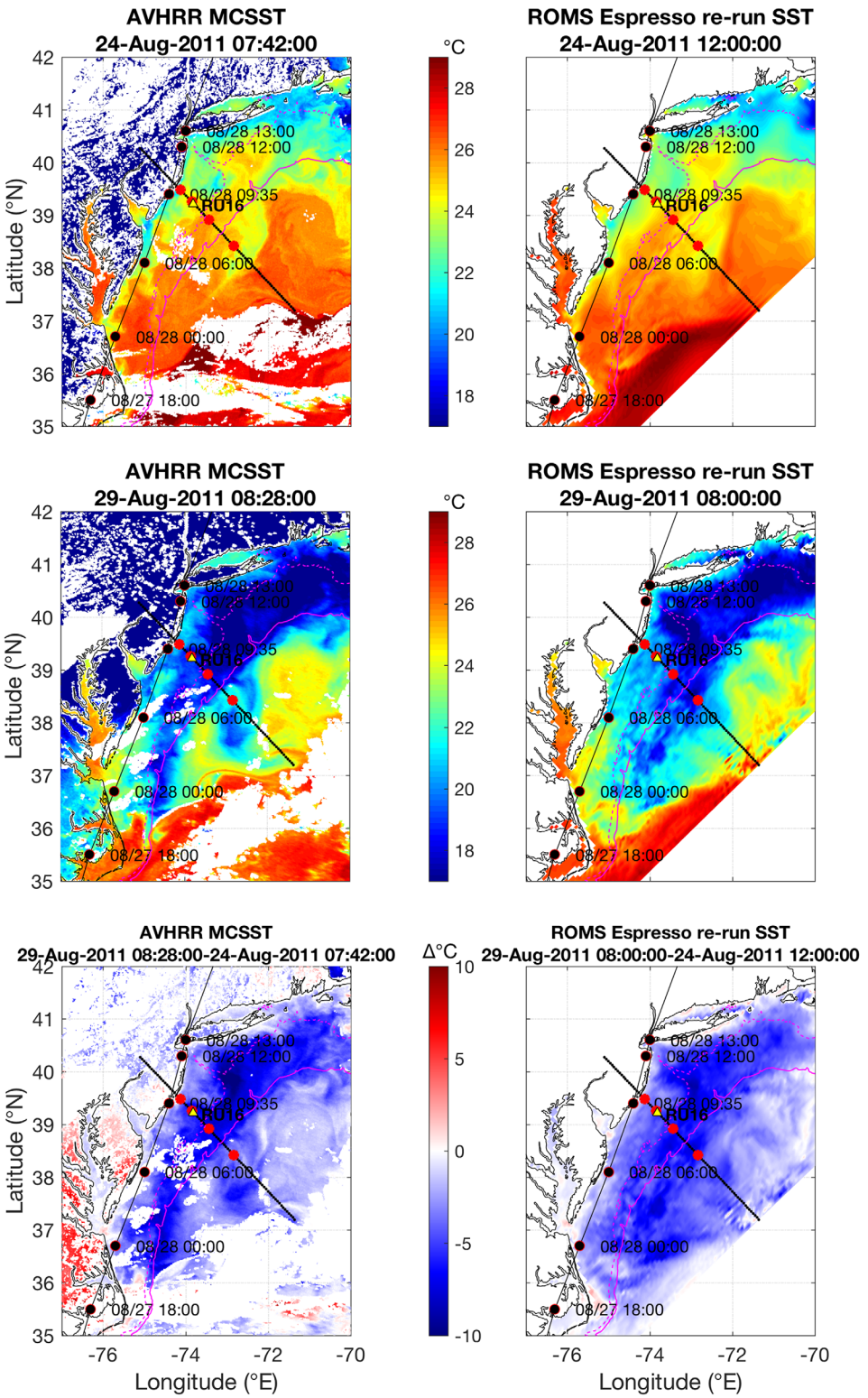


**Figure 3.** Irene. AVHRR Multi-Channel SST (MCSST) (top left) and ROMS ESPreSSO rerun SST (top right) prestorm for Irene; the same for poststorm in middle figures, and for poststorm minus prestorm in bottom figures. Dashed magenta contour is 50 m isobath, and solid magenta contour is 200 m isobath. RU16 location throughout the storm period plotted as yellow triangle, NHC best track for Irene in black with red outlined dots, small black dots in line northwest to southeast indicating cross-section location taken for Hövmoller figures below, and large red dots along this black line indicating profile locations taken for temperature diagnostic Figure 15.

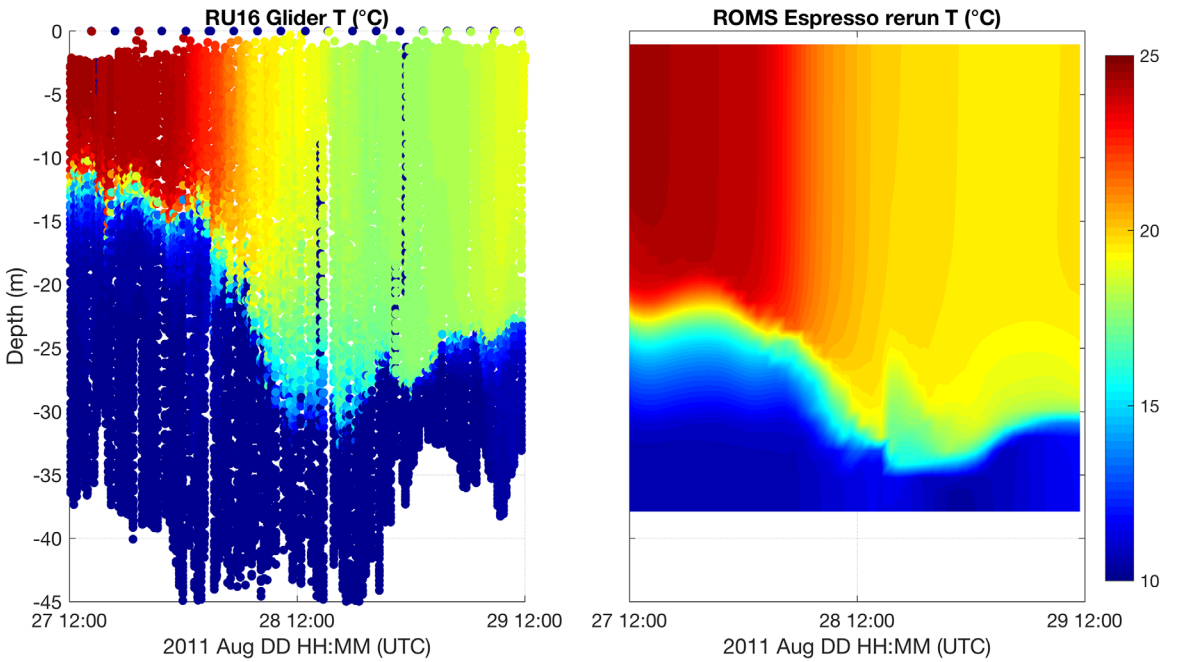


**Figure 4.** Irene. RU16 glider temperature (°C) (left) and ROMS ESPreSSO rerun temperature (°C) (right) at the closest ESPreSSO grid point to the average RU16 glider location during the storm.

thermocline is deeper than observed, the two-layer structure is present to support the relevant processes. Upon storm forcing, the ROMS thermocline deepens to the correct depth, but the surface does not sufficiently cool, likely due to the inadequate supply of cold bottom water at the start. Insufficient surface ocean cooling in model simulations due to an excessively thick surface layer has also been found to occur in other recent TC studies [e.g., *Zhang et al*., 2016], and is likely a common deficiency in numerical model simulations of TC ocean response. Despite deficiencies in the details, the overall storm response characteristics—two-layer structure at the start, deepening of the thermocline, and rapid and intense cooling of the surface mixed layer—are present and adequate for determining dominant force balances and diagnosing the causes of SST cooling.

### 3.2.2. ROMS Simulation Validation: Tropical Storm Barry (2007)

A prestorm map of SST over the MAB from AVHRR at 0559 UTC on 2 June 2007 (Figure 5, top left) is partially blocked by clouds but shows a warm Gulf Stream offshore, a couple Gulf Stream rings to the northwest in the slope water, a ribbon of colder water along the shelf break at 200 m, a ribbon of warmer water inshore of the 50 m isobath, and coastal upwelling east of Cape May, NJ, at the mouth of Delaware Bay, and along the Delmarva Peninsula. ROMS (Figure 5, top right) shows good agreement with AVHRR, with a warm Gulf Stream, cold water to the north, NJ and Delaware Bay coastal upwelling, warmer midshelf MAB waters, and a hint of the warm Gulf Stream filament approaching the 200 m isobath.

A poststorm map of SST over the MAB from AVHRR at 0207 UTC on 5 June 2007 (Figure 5, middle left) with the same color bar in Figure 5 (top) shows cooler water over the northern MAB, and ROMS at the same time (Figure 5, middle right) provides a similar picture. The difference maps of poststorm minus prestorm AVHRR SST (Figure 5, bottom left), ROMS rerun at the same time difference (Figure 5, bottom middle), and ROMS rerun to maximize cooling (Figure 5, bottom right) highlight the cooling and warming patterns across the MAB. Although clouds block parts of the map, AVHRR shows a pattern of warming in the southern MAB and offshore, and cooling in the northern MAB and offshore. Both ROMS rerun difference maps show more widespread cooling, with slight warming offshore NJ and off the Delmarva Peninsula, and where the Gulf Stream meanders moved through time.

Finally, the profile time series of temperature at the RU17 glider location (Figure 6, left) again shows surface mixed-layer cooling and deepening during the storm period, as in Figure 2. ROMS ESPreSSO rerun (Figure 6, right) shows a thermocline initially 15–20 m too deep, but surface and bottom temperatures overall correct.

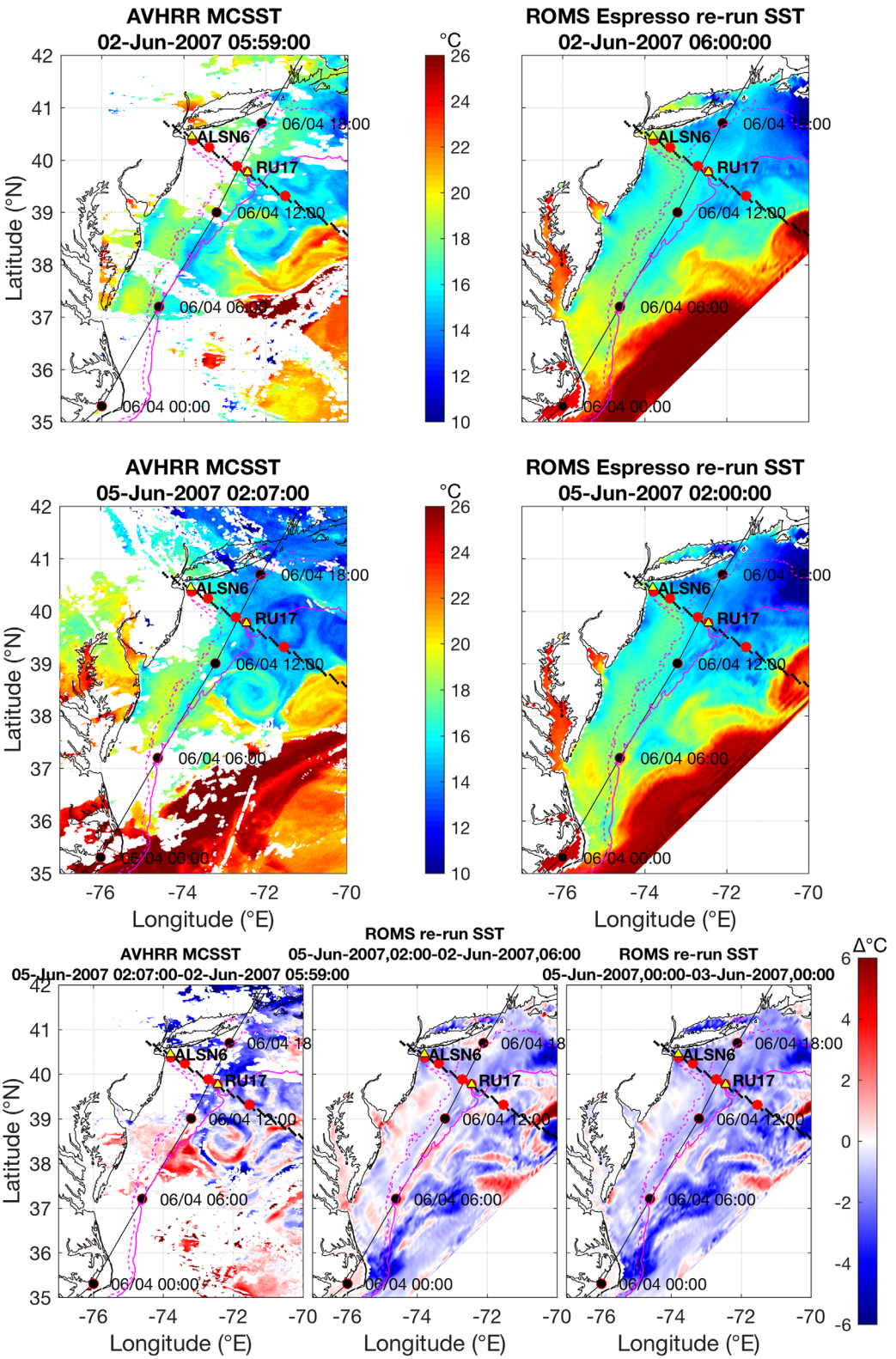


**Figure 5.** Barry. The same as Figure 3, but for Barry. NDBC station ALSN6 and RU17 glider locations indicated with yellow triangles. Northern cross-section location used for Barry plotted as west-northwest to east-southeast black dots just north of the Hudson Canyon, and large red dots along this black line indicating profile locations taken for temperature diagnostic Figure 16. A third figure on bottom (bottom right) is added for Barry with poststorm minus prestorm time difference chosen to maximize the cooling across the map in the ROMS ESPreSSO rerun.

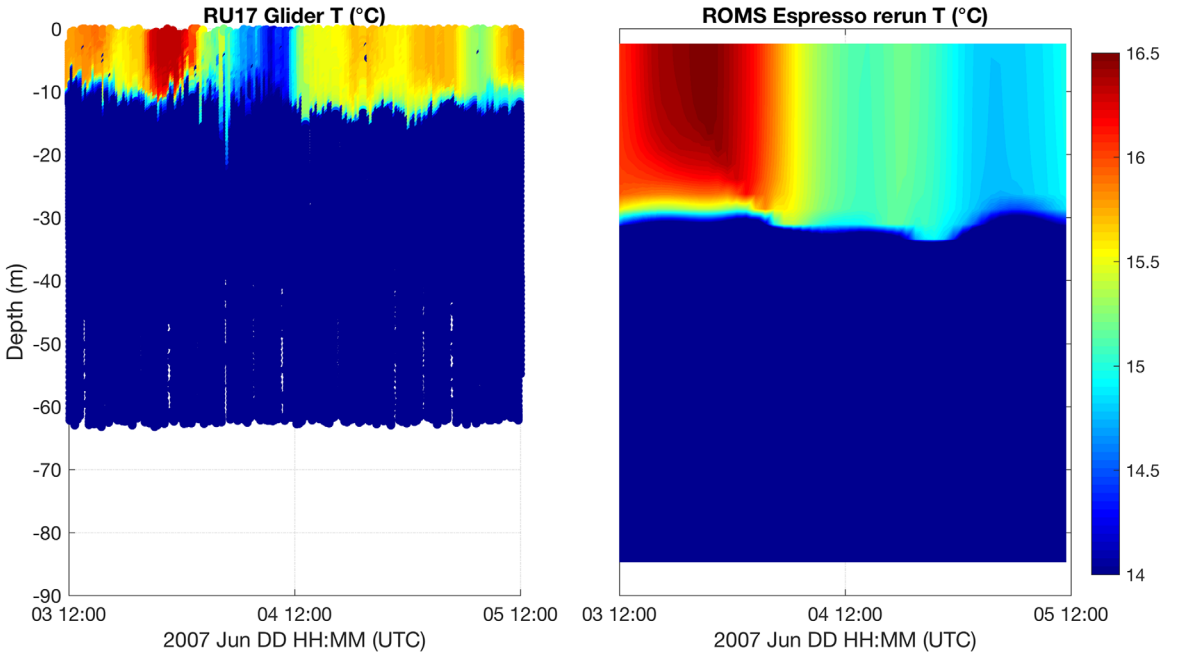


**Figure 6.** Barry. The same as Figure 4, but for RU17 glider in Barry. RU17 only sampled to ~60 m even though full water column depth was >80 m.

The resulting cooling of the surface layer occurs at about the correct time, but the surface layer warming poststorm does not occur.

### 3.2.3. Temperature, Current, Shear, and Momentum Balance Spatial Time Series: Irene

At the cross-section location near RU16 noted by the northwest to southeast black dots in Figure 3, Hövmoller diagrams of time (increasing up) versus distance offshore were produced. Surface temperature (Figure 7, top left) shows initially warm surface water stretching from the edge of the coastal upwelling to >200 km offshore. Then, SST rapidly cools across the shelf and in deep water, so that any cooling after eye passage (from NAM—two hours later than observed) is minimal. No SST cooling occurred within the nearshore coastal upwelling region. Bottom temperature (Figure 7, bottom left) shows a warm downwelling bulge during the storm, starting at the coastline and extending to close to 50 km offshore. The core of the MAB Cold Pool can be seen around 100 km offshore. Four sample locations are noted with the vertical solid lines labeled (1) in the upwelling region, (2) near RU16, (3) in the core of the Cold Pool, and (4) in deep water. These four locations will be used in the temperature diagnostic analysis (section 3.2.5).

A Hövmoller of cross-shelf surface currents (Figure 7, top middle) show onshore currents increasing at about 0000 UTC on 28 August, from about 50 km offshore across the shelf and into some of the deeper water. For Irene model results, currents in Earth coordinates are again rotated 31° clockwise from north to attain cross-shelf and along-shelf components. The onshore surface currents peak at around 0300 UTC and then decrease a few hours before eye passage. Bottom currents (Figure 7, bottom middle) are opposing offshore across the shelf and weaker than the onshore surface currents. The bottom onshore currents begin again at about 0000 UTC on 28 August and last until eye passage. After eye passage, surface currents switch to offshore, with the switch nearshore occurring a few hours after eye passage likely due to tidal influence (not shown). Bottom currents switch to onshore after eye passage almost immediately. Maximum shear from this plot occurred roughly from 0000 to 1200 UTC on 28 August and reversed from 1500 UTC on 28 August to 0000 UTC on 29 August.

The along-shelf surface current Hövmoller (Figure 7, top right) shows northeastward currents ahead of and after eye passage, with southwestward surface currents after eye passage in deeper water. Bottom currents (Figure 7, bottom right) are southwestward ahead of eye passage and immediately after, then northeastward later at 0000 UTC on 29 August. Maximum shear from this plot occurred roughly from 0600 to 1500 UTC on 28 August.

A bulk surface to bottom shear Hövmoller diagram, comprised the cross-shelf and along-shelf components, is shown in Figure 8 (left). This bulk shear Hövmoller shows a symmetric ~50% ahead and 50% behind eye

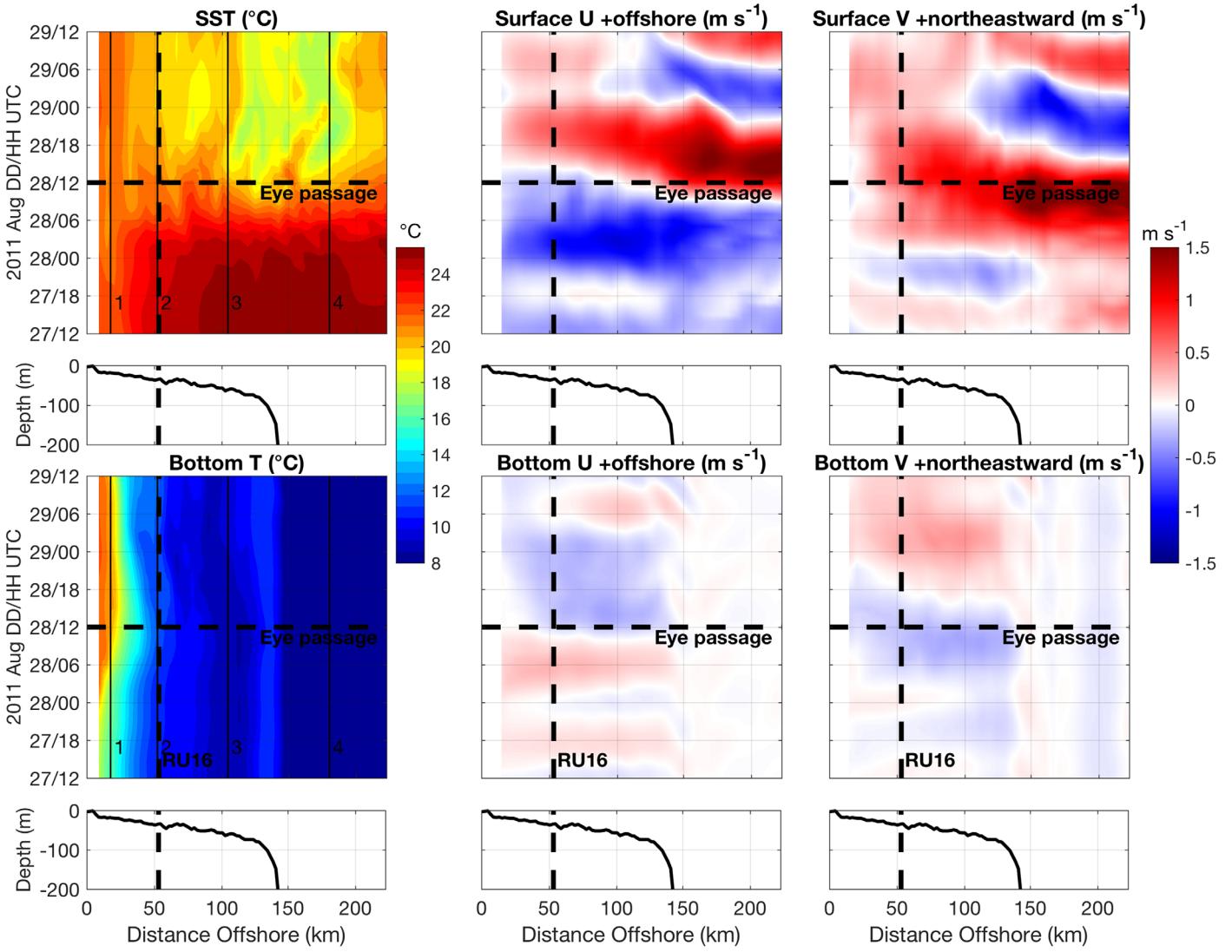


**Figure 7.** Irene. Hövmollers of ROMS ESPreSSO rerun SST (°C, top left), surface cross-shelf currents (m $s^{-1}$, top middle), and surface along-shelf currents (m $s^{-1}$, top right), with positive reds offshore/northeastward and negative blues onshore/southwestward for cross-shelf/along-shelf currents. Bottom row the same as top row but for the bottom of the water column. Eye passage in NAM atmospheric forcing marked with the horizontal dashed line, and RU16 glider location marked with the vertical dashed line. Vertical solid lines in left figure labeled 1 (upwelling), 2 (near RU16), 3 (in Cold Pool core), and 4 (in deep water) are locations where temperature diagnostics are performed in Figure 15. Water depth (m) along the cross section is plotted in the figures below the Hövmoller figures.

shear pattern in deep water, consistent with *Price* [1981]. In the shallow water over the continental shelf, shear is skewed ahead-of-eye-center. Because in deep water the bottom layer is quiescent and in shallow water the bottom layer is moving, only qualitative comparisons between deep and shallow water can be made. Additionally, bottom currents in shallow water are affected by opposing bottom stress, restricting any quantitative comparisons between deep and shallow water. By changing bottom currents to 0, a more evenly distributed shear pattern between ahead of and behind eye passage results (Figure 8, right), showing that the opposing bottom currents in the two-layer circulation has an influence on the shear pattern.

The ahead-of-eye-center cooling due to this shear is greater than behind-eye cooling (Figure 7, top left), potentially because (1) behind the eye center the water column is already mixed, and the surface layer is already deeper, (2) there are weaker backside offshore winds than frontside onshore winds due to frictional land effects—supported by observations at NDBC buoys 44014, 44009, and 44065, and at a WeatherFlow Inc. coastal land station at Tuckerton, NJ, and (3) the frontside of Irene cools the SST, the eye moves over the cooler water and weakens the storm, and the backside is weaker (Figure 1). As will be shown in the following momentum balance Hövmollers, the dominant cross-shelf momentum terms are onshore wind

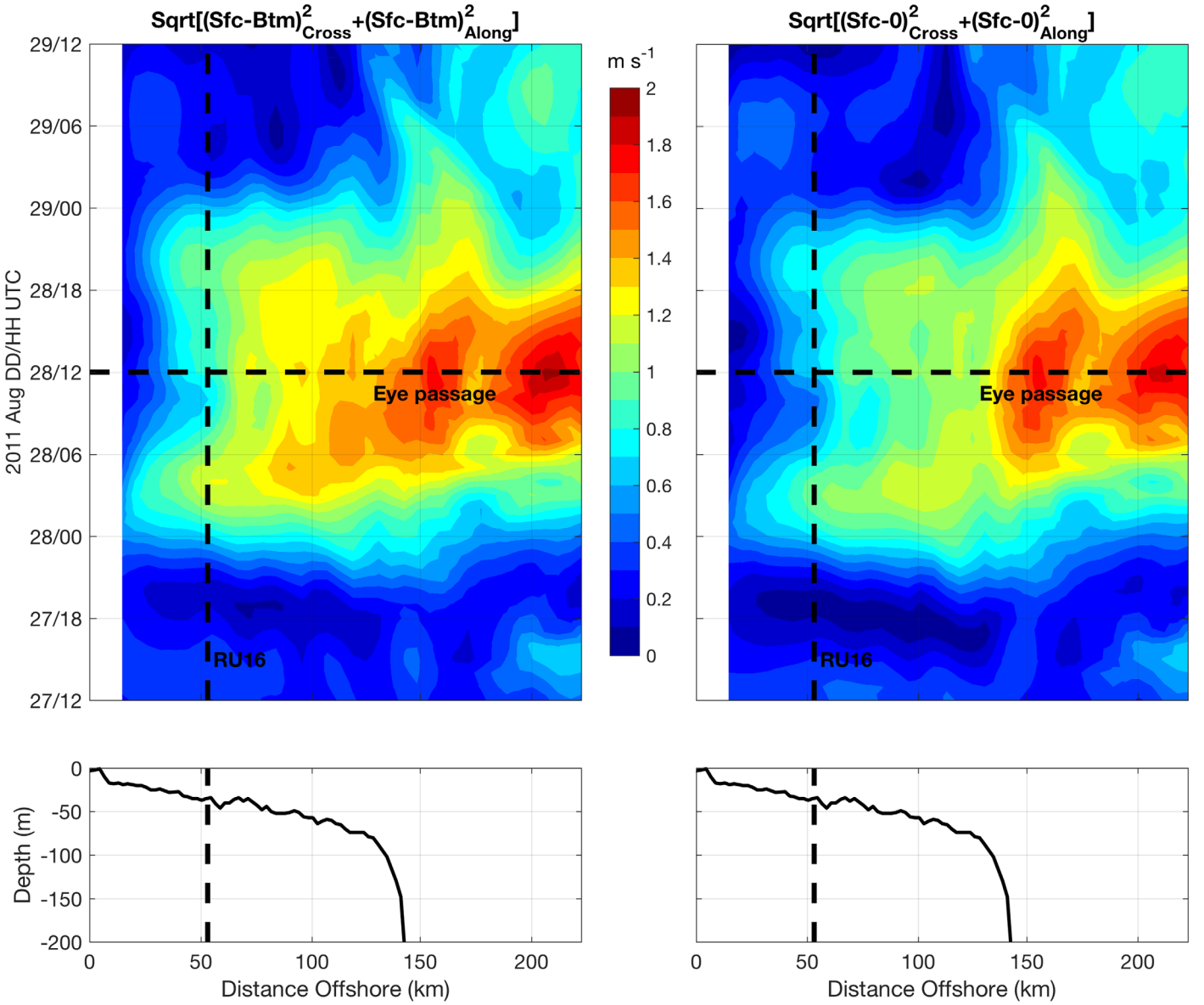


**Figure 8.** Irene. Same formatted Hövmoller as in Figure 7, but for bulk surface to bottom cross- and along-shelf shear (left, m s$^{-1}$). This bulk shear is calculated according to the equation in the header: square root of the sum of the squares of the surface to bottom cross-shelf and along-shelf shears. Right figure is the same as left but for 0 substituted for bottom currents.

stress balanced by offshore pressure gradient force ahead-of-eye-center, and offshore wind stress balanced by onshore pressure gradient force behind-eye-center. This balance is likely due to the presence of the coastline and shallow bottom, in which onshore surface winds ahead-of-eye-center pile water at the coast and result in the offshore bottom current, and offshore surface winds behind-eye-center push water away from the coast and result in the onshore bottom current. In both cases—ahead-of-eye-center and behind-eye-center—a two-layer circulation occurs due to the presence of the coastline, shallow bottom, and stratified water column.

The depth-averaged cross-shelf momentum balance time series (Figure 9) depicts all terms except for horizontal viscosity, which was very small. Acceleration shows a strongly tidal signal, with less onshore acceleration just before eye passage. Wind stress is strongly onshore ahead-of-eye passage, and switches to offshore after. Pressure gradient force is offshore ahead-of-eye-center from the coast all the way to the shelf break, and then switches to onshore midshelf first and then both nearshore and near the shelf break second; this pressure gradient pattern is due to coastal setup ahead-of-eye and coastal set down behind-eye.

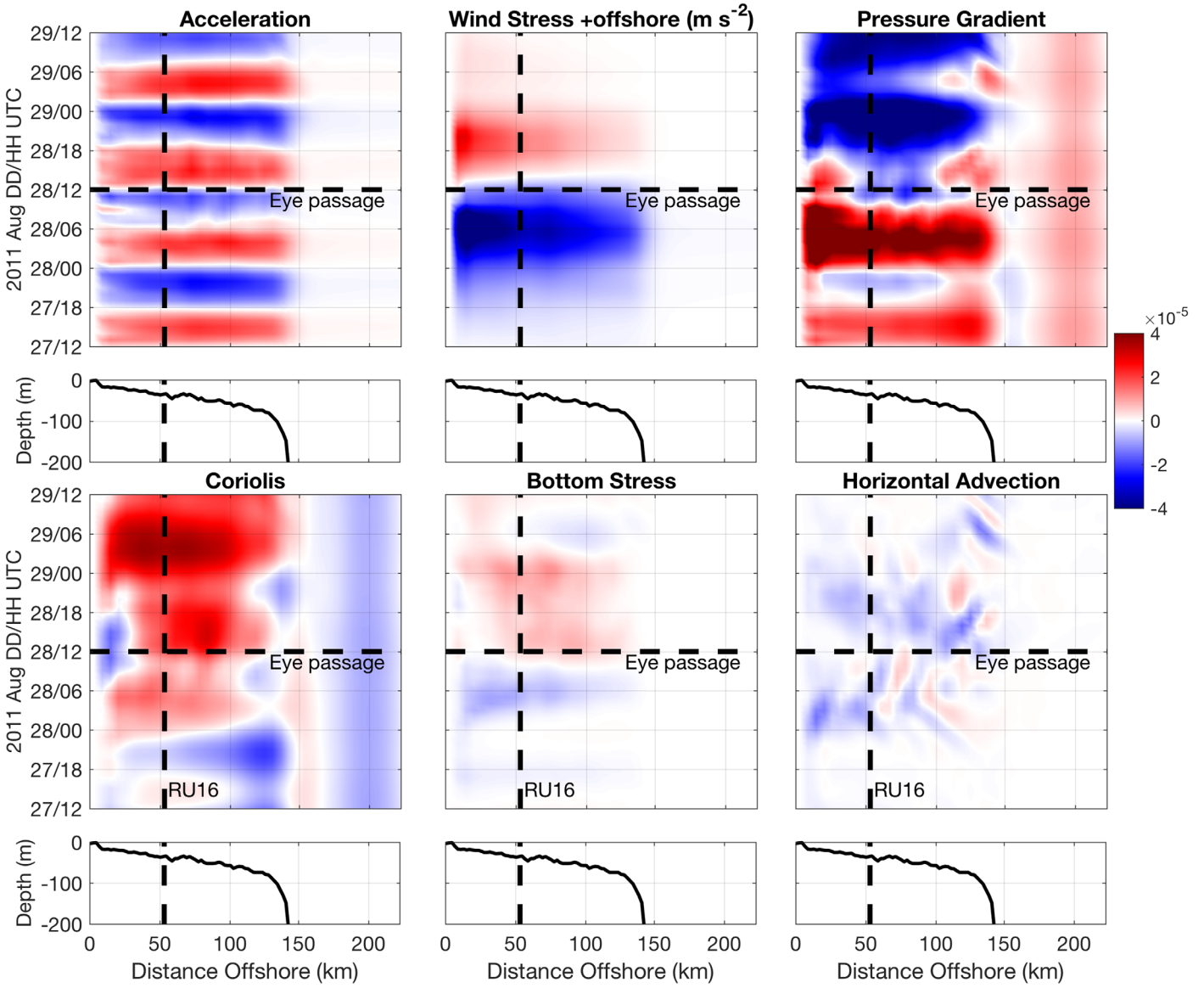


**Figure 9.** Irene. Hövmollers of the cross-shelf depth-averaged momentum balance terms (m $s^{-2}$), with positive reds offshore and negative blues onshore. Horizontal diffusion was small and thus not plotted.

Coriolis is offshore, increasing after the eye. Bottom stress is onshore opposing the offshore bottom currents ahead-of-eye, and then switches sign after eye. Finally, advection is small and noisy, with a response near the inertial period especially near the shelf break. The dominant cross-shelf force balance progresses from onshore wind stress balanced by offshore pressure gradient ahead-of-eye-center, to offshore wind stress and Coriolis balanced by onshore pressure gradient after eye passage until 0000 UTC on 29 August, and finally to a geostrophic balance of offshore Coriolis balanced by onshore pressure gradient.

In the along-shelf direction, depth-averaged momentum balance terms (Figure 10) are generally smaller than the cross-shelf terms. Again, acceleration has a tidal signal, but so does Coriolis. The dominant along-shelf force balance progresses from southwestward wind stress balanced by northeastward pressure gradient and Coriolis, to northeastward wind stress balanced by southwestward pressure gradient and Coriolis, and finally to alternating southwestward and northeastward pressure gradient balanced by Coriolis (tidal periodicity).

#### 3.2.4. Temperature, Current, Shear, and Momentum Balance Spatial Time Series: Barry

The time series of SST for Barry (Figure 11, top left) was taken at the northern WNW to ESE cross-section location just north of the Hudson Canyon as indicated by the black dots in Figure 5. This northern location

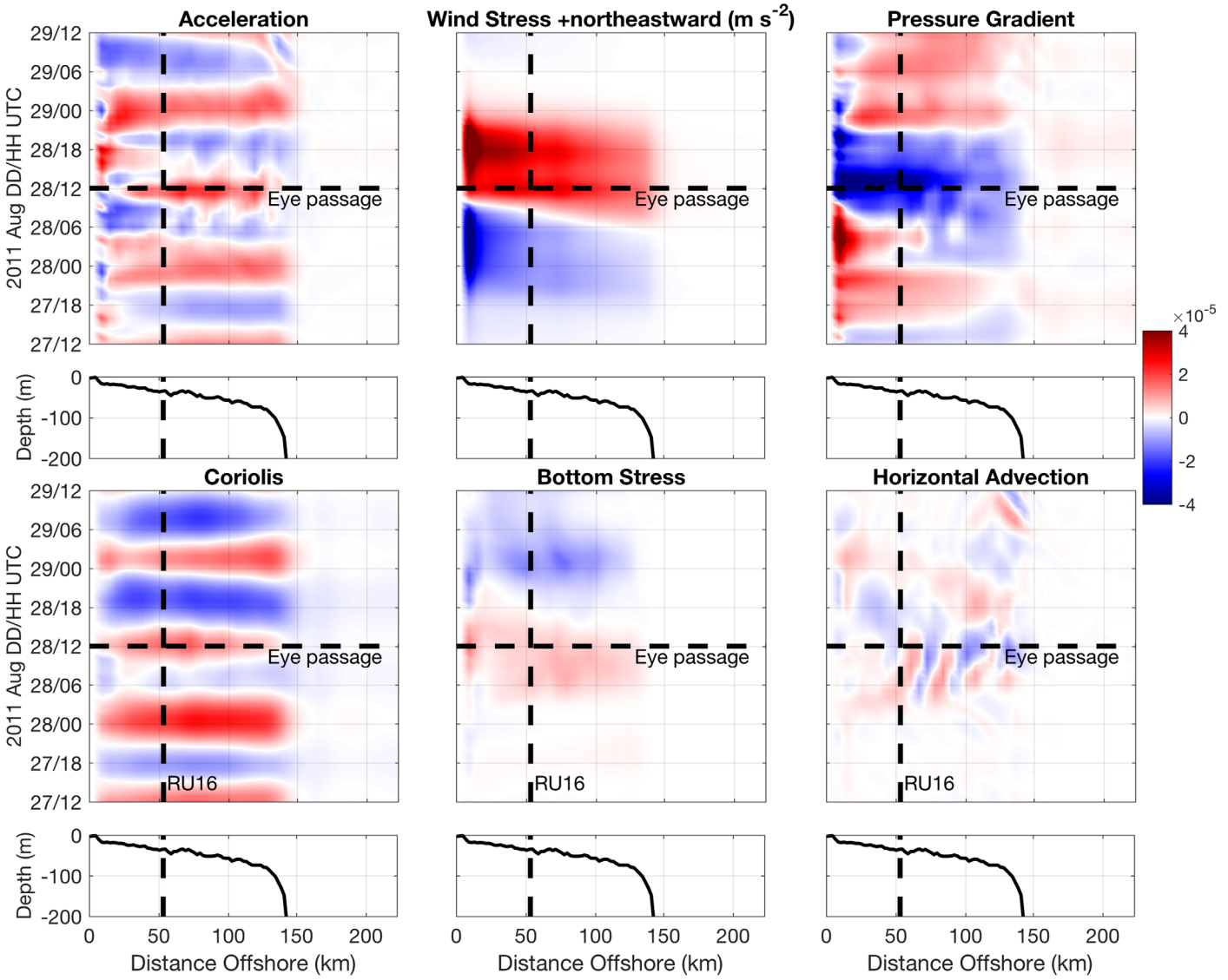


**Figure 10.** Irene. Same as Figure 9 but for along-shelf depth-averaged momentum balance terms (m $s^{-2}$), with positive reds northeastward and negative blues southwestward.

was chosen to target the greatest SST cooling in Barry. A similar cooling signal is apparent across the shelf and even in deep water. At National Data Buoy Center (NDBC) station ALSN6, the Barry station used by *Glenn et al.* [2016] for the ahead-of-eye-center cooling signal, cooling (~3.5°C) was greatest. At the warm strip of water indicated by the vertical line labeled "2," and in the deep water, total cooling was less than 1°C. The bottom temperature spatial time series (Figure 11, bottom left) shows a similar but more subtle downwelling bulge from the coast as was evident in Irene. Five sample locations are noted with the vertical solid lines labeled (1) in the nearshore maximum cooling and near ALSN6, (2) in the warm strip of water, (3) in the core of the Cold Pool, (4) near RU17, and (5) in deep water. These five locations will be used in the temperature diagnostic analysis (section 3.2.6).

The cross-shelf surface current time series (Figure 11, top middle) shows onshore surface currents peaking 12–18 h prior to eye passage, but remaining weakly onshore until eye passage. For Barry model results, currents in Earth coordinates are again rotated 51° clockwise from north to attain cross-shelf and along-shelf components. Bottom currents (Figure 11, bottom middle) show a primarily tidal signal, with alternative offshore and onshore bottom currents. Maximum shear was roughly 0600 to 1200 UTC on 4 June. This maximum shear occurs when the bottom offshore currents (mainly tidal) oppose the onshore surface currents. Because the storm forcing is weaker than in Irene, the tidal signal dominates the bottom current forcing.

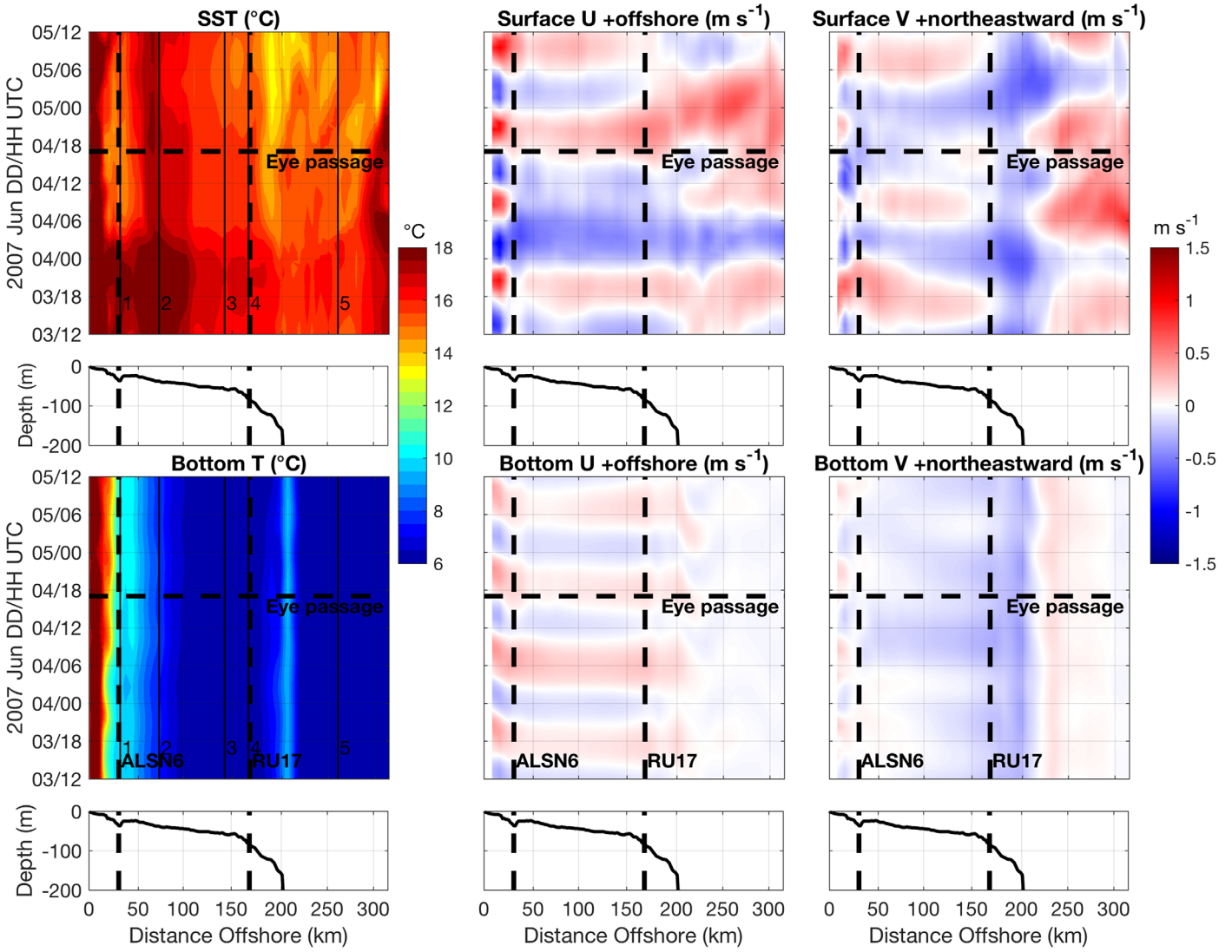


**Figure 11.** Barry. Same as Figure 7 but for Barry, with ALSN6 and RU17 locations plotted as vertical dashed lines. Vertical solid lines in left figures labeled 2 (near ALSN6), 2 (in warm strip), 3 (in Cold Pool core), 4 (near RU17), and 5 (in deep water) are locations where temperature diagnostics are performed in Figure 16.

This is consistent with the findings of *Keen and Glenn* [1995], who found that during a storm crossing the MAB in October 1990, the tidal signal dominated the bottom current forcing, and storm sedimentation was directly related to the tidal flow.

In the along-shelf direction, surface currents were northeastward before eye passage and southwestward after (Figure 11, top right). Bottom currents were southwestward the entire storm period, both before and after eye passage. A similar analysis just south of the Hudson Canyon may help answer why this occurred. One potential reason is that the Hudson Canyon acted as a barrier, blocking bottom currents from crossing the large bathymetric gradients.

The bulk surface to bottom shear Hövmoller for Barry, comprised the cross-shelf and along-shelf shears, is shown in Figure 12 (left). This bulk shear Hövmoller again shows a roughly symmetric ~50% ahead and 50% behind eye shear pattern in deep water if the time period of 0000 UTC on 4 June to 0600 UTC on 5 June is used. Again, like for Irene, shear is skewed ahead-of-eye passage in the shallow water, and by substituting 0 for bottom currents, a more (but not quite fully) symmetric shear pattern in shallow water results (Figure 12, right).

The Hövmoller cross-shelf depth-averaged momentum balance terms (Figure 13) show a strongly tidal signal in the acceleration, pressure gradient, and Coriolis terms across the shelf, and in the bottom stress and

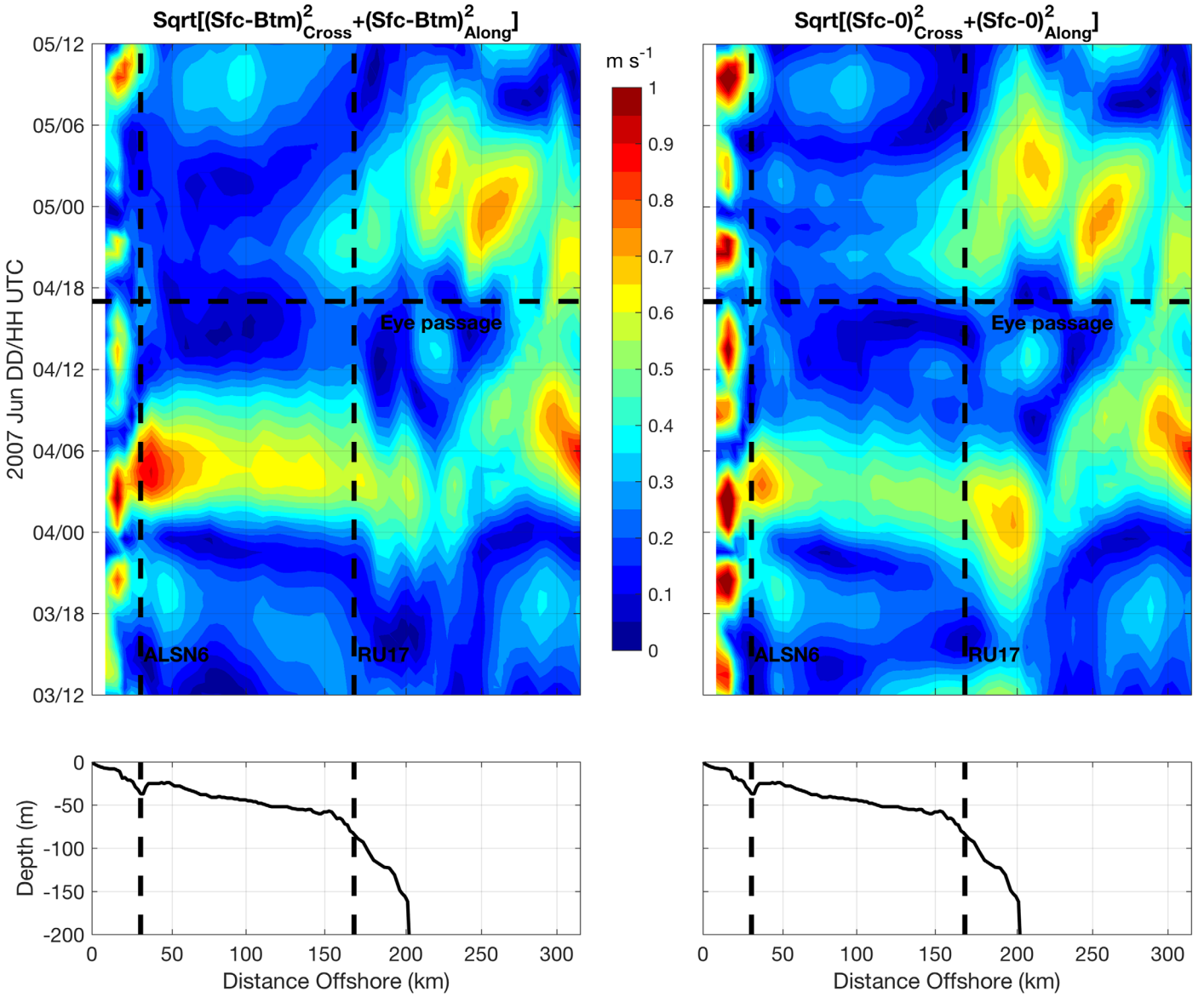


**Figure 12.** Barry. Same as Figure 8 (bulk surface to bottom shear analysis), but for Barry.

horizontal advection terms very near shore. Wind stress was directed onshore ahead of eye passage and weakly offshore after. Pressure gradient was primarily tidal, with more positive offshore values along the shelf break just ahead of eye passage as compared to after eye passage. Coriolis was largely tidal and onshore, with the maximum again at the shelf break. Bottom stress was mostly tidal, but mostly negative opposing the offshore bottom currents at about 0600 UTC on 4 June ahead of eye, when the downwelling circulation aligned with the tidal signal. Finally, horizontal advection was mostly small. The dominant depth-averaged cross-shelf force balance progressed from onshore wind stress balanced by offshore pressure gradient ahead of eye passage, to offshore wind stress balanced by alternating onshore/offshore Coriolis and pressure gradient (tidal periodicity) just after eye passage, to quasi-geostrophic balance with alternating onshore/offshore Coriolis balanced by pressure gradient (again tidal).

The Hövmoller along-shelf depth-averaged momentum balance terms (Figure 14) show a mostly tidally forced signature. Acceleration was mostly tidal, with slightly more negative onshore (or less positive offshore) acceleration ahead of eye passage from 0000 to ~0900 UTC on 4 June. Wind stress was southwestward ahead of eye passage and northeastward after. Pressure gradient and Coriolis terms were primarily

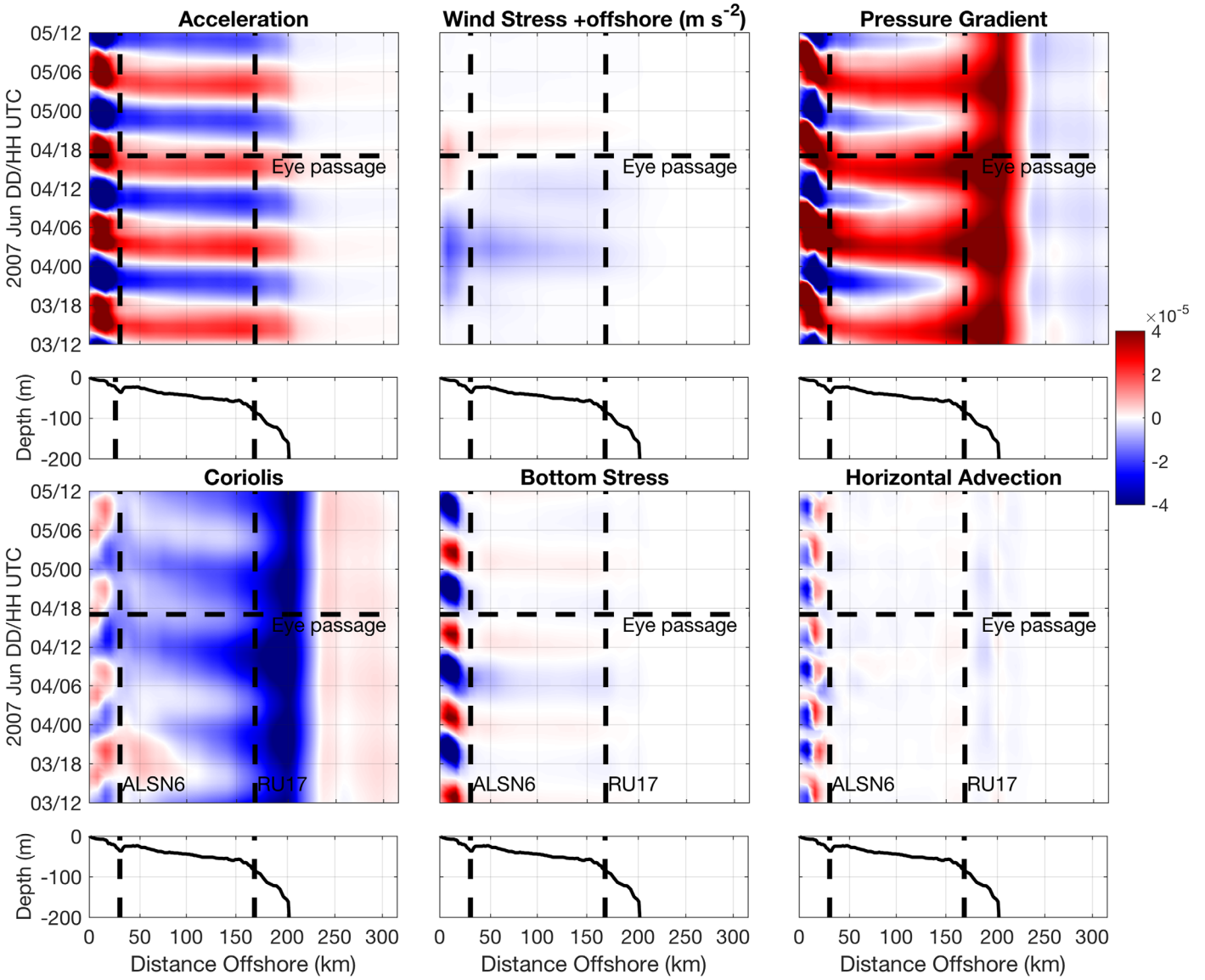


**Figure 13.** Barry. Same as Figure 9 (Hövmoller cross-shelf depth-averaged momentum balance terms), but for Barry.

tidal, bottom stress was always northeastward opposing the southwestward bottom currents, and horizontal advection was small. The dominant along-shelf depth-averaged momentum balance progressed from southwestward wind stress balanced by northeastward bottom stress and a residual in the alternating northeastward/southwestward pressure gradient term and Coriolis term ahead of eye passage, to northeastward wind stress balanced by alternating northeastward/southwestward Coriolis and pressure gradient behind eye passage.

The shelf break maxima in the pressure gradient and Coriolis terms could be due to the presence of a warm core ring starting prestorm just north of the Hudson Canyon and the northern cross-section location (Figure 5, top left) and moving southeastward by poststorm (Figure 5, middle left). This ring, moving along the shelf break and beginning to impinge onto the shelf, forces a geostrophic circulation at the shelf break front [*Zhang and Gawarkiewicz*, 2015], which is evident at the shelf break in both the cross-shelf and along-shelf momentum balance Hövmollers (Figures 12 and 13).

### 3.2.5. Advection Versus Mixing Temperature Response: Irene

The temperature diagnostic equation terms were plotted for Irene (Figure 15) at the points indicated by the large red dots in Figure 3 and by the vertical solid black lines in Figure 7 (left) to determine the primary

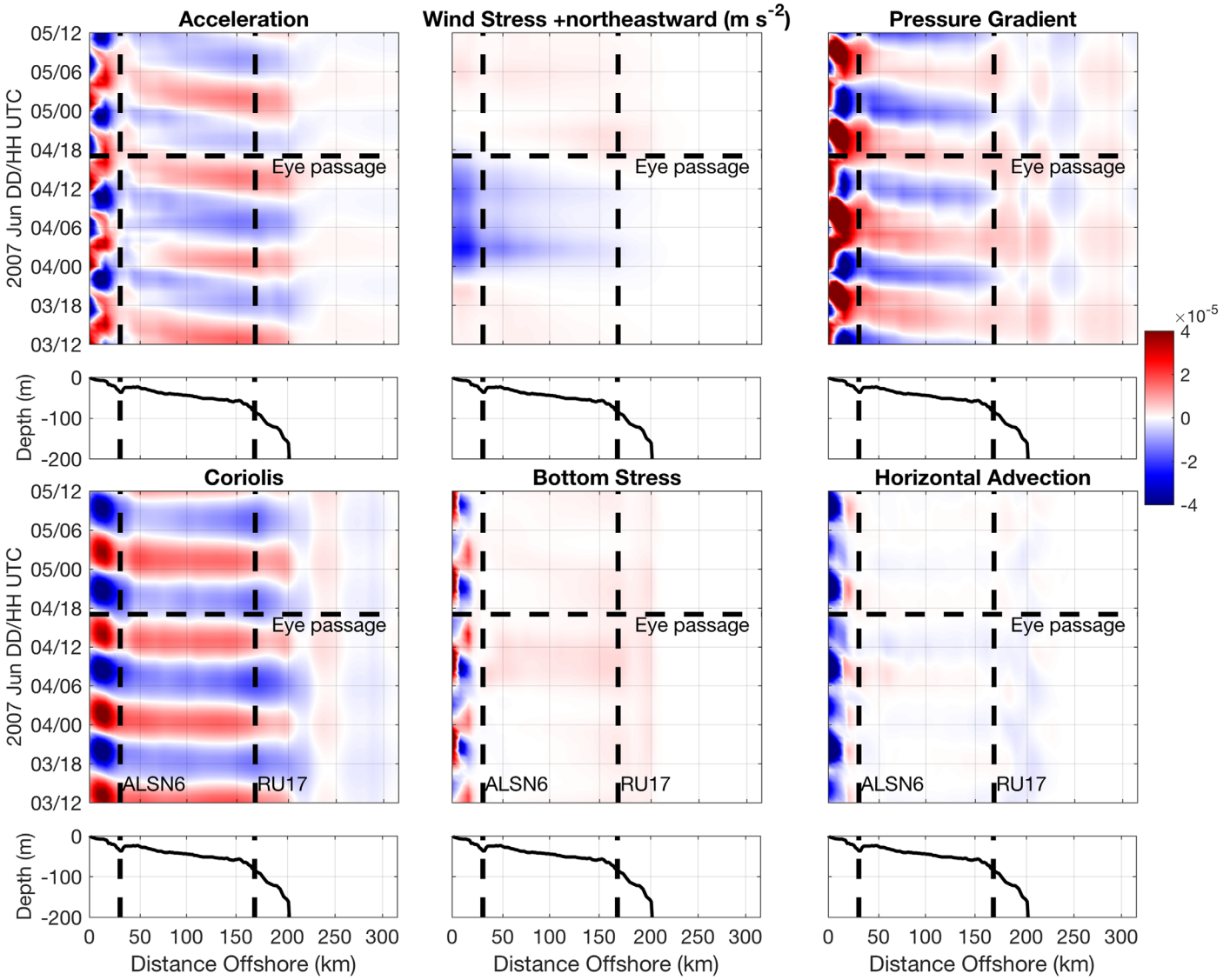


**Figure 14.** Barry. Same as Figure 10 (Hövmoller along-shelf depth-averaged momentum balance terms), but for Barry.

cause of cooling. The left figure is within the upwelling region, the second is at RU16, the third is in the MAB Cold Pool core, and the fourth is in deep water. At the top is the full temperature rate term, in the middle is the vertical diffusion term, and at the bottom are the vertical plus horizontal advection terms. Horizontal diffusion was not plotted, as it was very small. First, a general tidal signal is apparent in the full temperature rate term, primarily due to advection at all four locations. Cooling in the mixed layer was due to vertical diffusion at all four points, with ahead-of-eye-center cooling occurring at points 1–3. At point 1 within the upwelling, surface mixed-layer cooling stopped once the thermocline reached the bottom of the water column, as the source of cold water was removed (Figure 15, left middle). At point 2 near RU16, ahead-of-eye-center cooling was caused by vertical diffusion cooling being skewed ahead-of-eye-center. At point 3 in the Cold Pool core, vertical diffusion cooling was also skewed ahead-of-eye-center, with advection warming after eye passage. Finally, at point 4 in the deep water, a deep, cold quiescent bottom allowed for some cold water to entrain into the thick ~200 m surface mixed-layer ahead-of-eye passage, with an advective signal dominating after eye passage.

### 3.2.6. Advection Versus Mixing Temperature Response: Barry

The temperature diagnostic equation terms plotted for Irene at four locations in Figure 15 were also plotted for Barry at five locations in Figure 16. These five locations are indicated by the large red dots in Figure 5

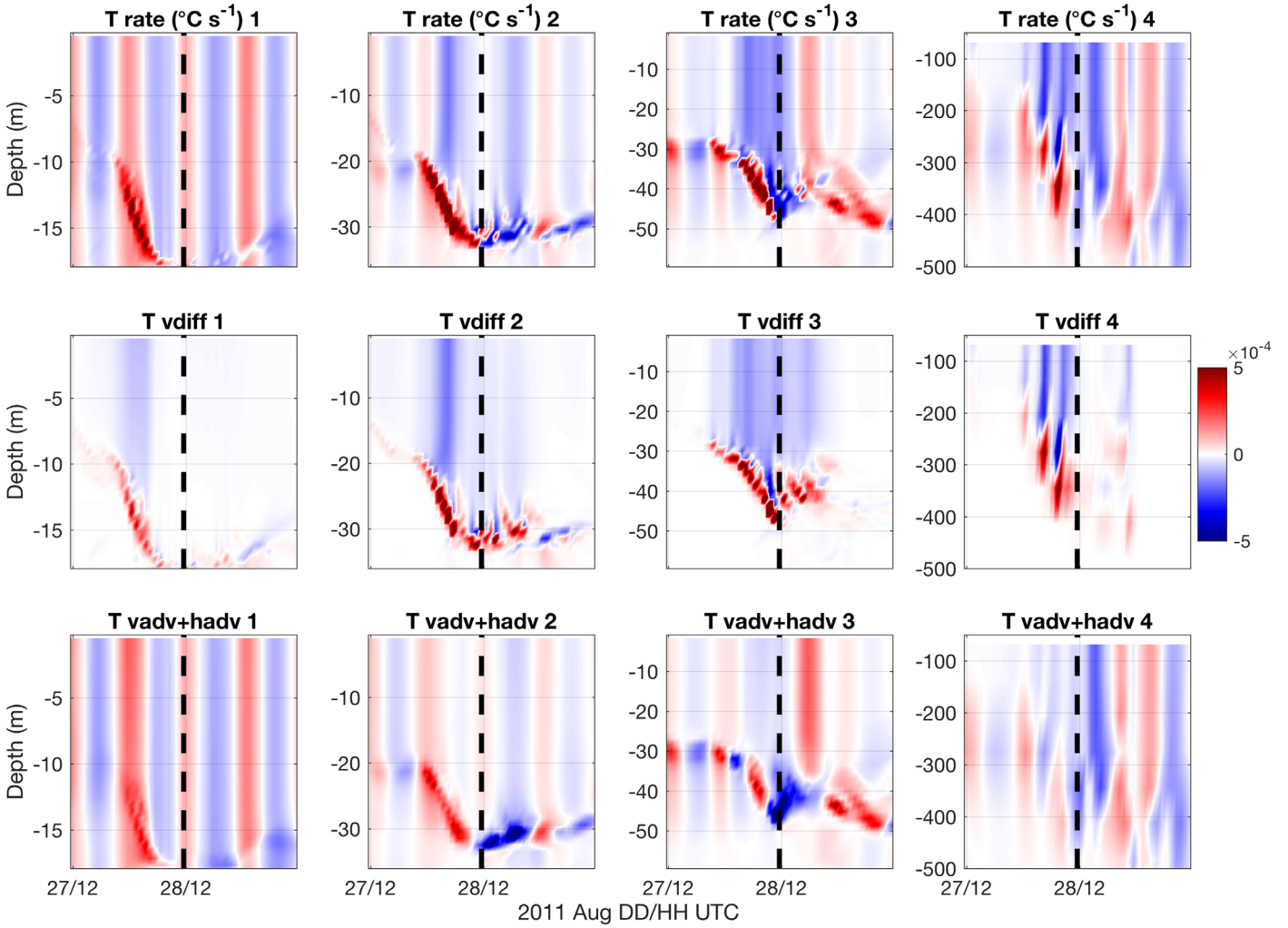


**Figure 15.** Irene. Temperature diagnostic equation terms at points 1–4 marked in Figure 3 red dots ordered 1–4 northwest to southeast, and in Figure 7 (left), with full temperature rate term at top, vertical diffusion in middle, and vertical + horizontal advection at bottom (°C $s^{-1}$). Horizontal diffusion is small and thus not plotted. Eye passage marked with vertical dashed line. At point 4, only the top 500 m of the water column is plotted.

and the vertical solid black lines in Figure 11 (left). For Barry, Figure 16 (left) is near ALSN6, the second figure is within the warm strip of water, the third figure is within the Cold Pool core, the fourth is near RU17, and the fifth is in deep water. Again, a tidal advection signal is apparent, with vertical diffusion not exhibiting any tidal cooling/warming signal. Vertical diffusion again caused cooling in the mixed layer except at point 5 in the deep water. Point 5 looks primarily advective with a deep quiescent bottom. At points 1–4 the tidal advection cooling/warming periodicity was modulated by the vertical diffusion cooling, which looks to be skewed ahead-of-eye passage during the greatest shear period (Figure 12, left).

## 4. Summary

Baroclinic coastal ocean cooling processes were investigated in detail for Hurricane Irene (2011) and Tropical Storm Barry (2007), two summer TCs, both with rapid ahead-of-eye-center cooling, but with different tracks and occurring at different times in the summer season. Cross-shelf variability in the depth-averaged momentum balance terms demonstrated that the dominant force balance driving the baroclinic circulation was the same across the entire MAB shelf. Cross-shelf variability in the temperature diagnostic equations showed that the resultant ahead-of-eye-center cooling of the surface layer in both storms was dominated by mixing rather than advection.

For Irene, it was previously found that cross-shelf two-layer surface to bottom opposing current shear was large and along-shelf surface to bottom shear was small at the RU16 glider location [*Glenn et al.*, 2016]. Here

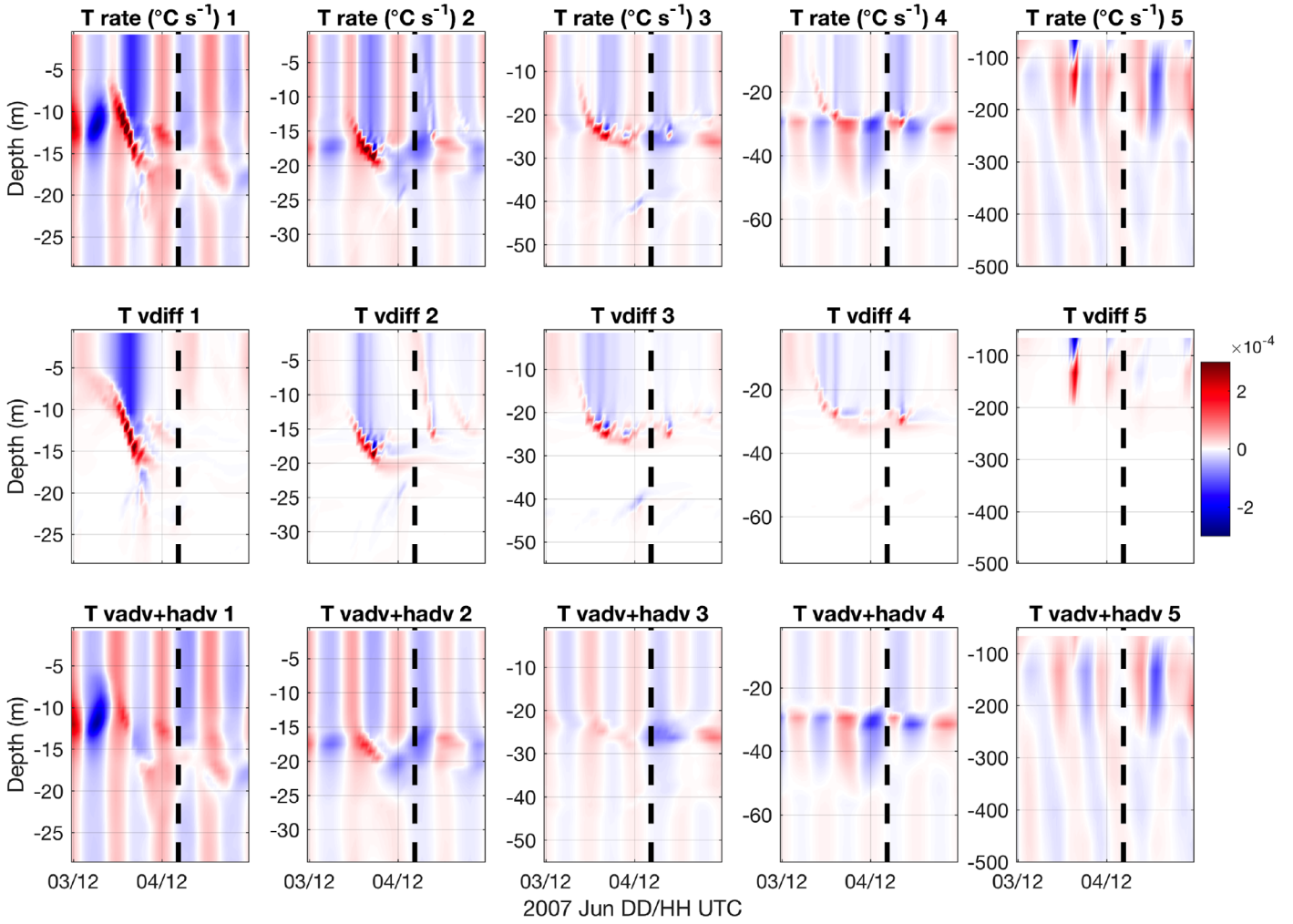


**Figure 16.** Barry. Same as Figure 15 (temperature diagnostic equation terms) but for Barry. Points 1–5 are marked in Figure 5 red dots ordered 1–5 west-northwest to east-southeast, and in Figure 11 (left).

for Barry, it was found that both the cross-shelf and along-shelf components of the surface to bottom opposing current shear contributed to the mixing and cooling observed at the RU17 glider location. For both storms, analysis of bulk shear (including both cross-shelf and along-shelf shear components) indicated a symmetric 50% ahead and 50% behind eye shear pattern in deep water, but with maximum shear skewed ahead-of-eye-center in the shallow water over the continental shelf. This ahead-of-eye-center skewing of the vertical shear was found to occur not only due to opposing bottom currents over the shelf before the eye, but also due to weaker winds and a deeper surface layer after the eye.

For Irene, the dominant force balance ahead of eye passage was onshore wind stress balanced by offshore pressure gradient, and the large offshore pressure gradient term stretched across the entire shelf. The wind stress and pressure gradient terms switched directions right after eye passage and eventually the force balance evolved to geostrophic long after the storm. For Barry, the dominant force balance on the shelf ahead of eye passage was modulated by the tides but also had the onshore wind stress term balanced by offshore pressure gradient, and again the large offshore pressure gradient term extended all the way across the shelf. The along-shelf force balance also played a role for Barry, potentially due to the location of the cross section relative to the changing slopes of the bathymetry just north of the Hudson Canyon. In both the cross-shelf and along-shelf directions, independent of the wind forcing, there was a maximum in the pressure gradient and Coriolis terms near the shelf break, which coincided with a warm eddy moving southwestward along the shelf slope front with a geostrophic circulation.

Finally, cross-shelf variability in the temperature change diagnostic terms was investigated. For both storms in the shallow water on the shelf, vertical diffusion was the main cause of the mostly ahead-of-eye-center cooling in the surface mixed layer. Tidal periodicity of cooling/warming was apparent in the combined vertical and horizontal advection terms. Cooling in the surface layer due to vertical diffusion did occur within the coastal upwelling during Irene, and the cooling stopped once the thermocline hit the bottom of the water column as the bottom cold water was also removed. In deep water, vertical diffusion and advection were important drivers of mixed-layer cooling for Irene, whereas for Barry in deep water, advection was the main driver in the periodic and alternating warming/cooling near the surface.

The drivers for the major differences in coastal ocean response between Irene and Barry were storm track, structure, intensity, and time of year. Irene had a more inshore MAB track during the late summer stratified season, whereas Barry was weaker with a farther offshore track during the early summer stratified season. Due to the offshore track, MAB surface winds for Barry had a more along-shelf component than the primarily cross-shelf winds during Irene, leading to both cross-shelf and along-shelf components playing a larger role in the coastal ocean response for Barry, and a primarily cross-shelf response for Irene.

## 5. Discussion

*Glenn et al*. [2016] identified 11 summer storms that traversed northeastward across the MAB and that exhibited a range of ahead-of-eye-center cooling. Here we selected two extreme cases—both with an underwater glider deployed—from this envelope: one with an offshore track and the other with an inshore one. One was near the beginning of the summer stratified season and the other near the end. Indeed, differences in the details exist between the two storm extremes—from the along-shore component playing a larger role in Barry's force balance, to the alternating warming/cooling advective tidal signal playing a larger role in Barry's temperature response. Nevertheless, both storms exhibited a two-layer baroclinic circulation, forced by an offshore pressure gradient opposing the onshore wind stress ahead-of-eye-center and extending across the entire MAB shelf. Cooling in both storms was mostly ahead-of-eye-center and dominated by vertical shear-induced mixing. These commonalities across the two storm extremes indicate that the process is robust and can be expected on stratified continental shelves over a wide range of TC scenarios.

Because this process is robust across these two extreme cases drawn from the 30 year envelope of MAB summer cyclones, it will be critical to resolve and forecast the same process for future storms, with the goal of lowering the uncertainty in predictions of TC impacts. Realistic 3-D coupled models that assimilate coastal observatory data and that are capable of predicting the ahead-of-eye-center stratified coastal ocean cooling processes will be critical [e.g., *Zambon et al*., 2014; *Warner et al*., 2017]. The increasingly populated [*Peduzzi et al*., 2012] at-risk coastlines—the Northeast U.S. and northeastern China and Korea—adjacent to the two most stratified seas in the world—the MAB and Yellow Sea—will be increasingly vulnerable to TCs as sea levels rise [*Hansen et al*., 2016], as TCs more frequently and severely undergo rapid intensification just before landfall [*Emanuel*, 2017], and if maximum TC intensities continue to migrate poleward [*Kossin et al*., 2014]. By lowering uncertainty in coastal TC intensity forecasts through models that resolve these stratified coastal ocean cooling processes, these populations can better prepare for and respond to these rising threats.

**Acknowledgments**

HF Radar, glider, and satellite SST data used in this study are available through the MARACOOS assets page http://maracoos.org/data, https://rucool.marine.rutgers.edu/data, and http://marine.rutgers.edu/cool/auvs/index.php?did=369 with more detailed data sets available upon request to gregory.seroka@noaa.gov. Regional Ocean Modeling System results are also available upon request to gregory.seroka@noaa.gov. NAM data sets are publicly available through https://www.ncdc.noaa.gov/data-access/model-data/model-datasets/north-american-mesoscale-forecast-system-nam. Support was provided by New Jersey Board of Public Utilities (2010RU-COOL, BP-070), the Environmental Protection Agency (EP-11-C-000085), New Jersey Department of Environmental Protection (WM13–019-2013), National Oceanic and Atmospheric Administration (NOAA) led Integrated Ocean Observing System through the Mid-Atlantic Regional Association Coastal Ocean Observing System (MARACOOS, NA11NOS0120038), NOAA Cooperative Institute for the North Atlantic Region (NA13OAR4830233), and Rutgers University. We would like to thank John Wilkin and Julia Levin at Rutgers University for their suggestions regarding the ocean modeling, the Rutgers Ocean Modeling research associates for their ROMS help, and Rich Dunk for his helpful meteorological discussions and ideas.

## References

Cangialosi, J. P., and J. L. Franklin (2016), National Hurricane Center forecast verification report: 2015 hurricane season, National Hurricane Center, Miami, Fla.

D'Asaro, E., T. B. Sanford, P. P. Niiler, and E. J. Terrill (2007), Cold wake of Hurricane Frances, *Geophys. Res. Lett.*, *34*, L15609, doi:10.1029/2007GL030160.

Davis, R. E., C. C. Eriksen, and C. P. Jones (2002), Autonomous Buoyancy-driven underwater gliders, in *Technology and Applications of Autonomous Underwater Vehicles*, edited by G. Griffiths, pp. 37–58, CRC Press, London, New York.

DeMaria, M., C. R. Sampson, J. A. Knaff, and K. D. Musgrave (2014), Is tropical cyclone intensity guidance improving?, *Bull. Am. Meteorol. Soc.*, *95*(3), 387–398, doi:10.1175/BAMS-D-12-00240.1.

Emanuel, K. (2017), Will global warming make hurricane forecasting more difficult?, *Bull. Am. Meteorol. Soc.*, March 2017, pp. 495–502, doi:10.1175/BAMS-D-16-0134.1.

Fairall, C. W., E. F. Bradley, J. E. Hare, and A. A. Grachev (2003), Bulk parameterization of air-sea fluxes: Updates and verification for the COARE algorithm, *J. Clim.*, *16*(4), 571–591.

Glenn, S., C. Jones, M. Twardowski, L. Bowers, J. Kerfoot, J. Kohut, D. Webb, and O. Schofield (2008), Glider observations of sediment resuspension in a Middle Atlantic Bight fall transition storm, *Limnol. Oceanogr.*, *53*(5), 2180–2196, doi:10.4319/lo.2008.53.5_part_2.2180.

Glenn, S. M., T. N. Miles, G. N. Seroka, Y. Xu, R. K. Forney, F. Yu, H. Roarty, O. Schofield, and J. Kohut (2016), Stratified coastal ocean interactions with tropical cyclones, *Nat. Commun.*, *7*, 1–10, doi:10.1038/ncomms10887.

Haidvogel, D. B. et al. (2008), Ocean forecasting in terrain-following coordinates: Formulation and skill assessment of the Regional Ocean Modeling System, *J. Comput. Phys.*, *227*(7), 3595–3624, doi:10.1016/j.jcp.2007.06.016.

Hansen, J. et al. (2016), Ice melt, sea level rise and superstorms: Evidence from paleoclimate data, climate modeling, and modern observations that 2°C global warming could be dangerous, *Atmos. Chem. Phys.*, *16*(6), 3761–3812, doi:10.5194/acp-16-3761-2016.

Houghton, R. W., R. Schlitz, R. C. Beardsley, B. Butman, and J. L. Chamberlin (1982), The Middle Atlantic Bight cold pool: Evolution of the temperature structure during summer 1979, *J. Phys. Oceanogr.*, *12*(10), 1019–1029, doi:10.1175/1520-0485.

Hsu, S. A., and Z. Yan (1998), A note on the radius of maximum wind for hurricanes, *J. Coastal Res.*, *14*(2), 667–668.

Jaimes, B., and L. K. Shay (2015), Enhanced wind-driven downwelling flow in warm oceanic Eddy features during the intensification of Tropical Cyclone Isaac (2012): Observations and theory, *J. Phys. Oceanogr.*, *45*(6), 1667–1689, doi:10.1175/JPO-D-14-0176.1.

Keen, T. R., and S. M. Glenn (1995), A coupled hydrodynamic-bottom boundary layer model of storm and tidal flow in the Middle Atlantic Bight of North America, *J. Phys. Oceanogr.*, *25*(3), 391–406.

Kim, H. S., C. Lozano, V. Tallapragada, D. Iredell, D. Sheinin, H. L. Tolman, V. M. Gerald, and J. Sims (2014), Performance of ocean simulations in the coupled HWRF-HYCOM model, *J. Atmos. Oceanic Technol.*, *31*(2), 545–559, doi:10.1175/JTECH-D-13-00013.1.

Kossin, J. P., K. Emanuel, and G. Vecchi (2014), The poleward migration of the location of tropical cyclone maximum intensity, *Nature*, *509*(7500), 349–352, doi:10.1038/nature13278.

Lin, I.-I., C.-H. Chen, I.-F. Pun, W. T. Liu, and C.-C. Wu (2009), Warm ocean anomaly, air sea fluxes, and the rapid intensification of Tropical Cyclone Nargis (2008), *Geophys. Res. Lett.*, *36*, L03817, doi:10.1029/2008GL035815.

Mei, W., C. Pasquero, and F. Primeau (2012), The effect of translation speed upon the intensity of tropical cyclones over the tropical ocean, *Geophys. Res. Lett.*, *39*, L07801, doi:10.1029/2011GL050765.

Miles, T., S. Glenn, and O. Schofield (2013), Temporal and spatial variability in fall storm induced sediment resuspension on the Mid-Atlantic Bight, *Cont. Shelf Res.*, *63*, S36–S49.

Miles, T. N., G. N. Seroka, J. T. Kohut, O. Schofield, and S. M. Glenn (2015), Glider observations and modeling of sediment transport in Hurricane Sandy, *J. Geophys. Res. Oceans*, *120*, 1771–1791, doi:10.1002/2014JC010474.

NOAA National Centers for Environmental Information (2016), U.S. coastal relief model, NOAA, Boulder, Colo. [Available at http://www.ngdc.noaa.gov/mgg/coastal/crm.html.]

Peduzzi, P., B. Chatenoux, H. Dao, A. De Bono, C. Herold, J. Kossin, F. Mouton, and O. Nordbeck (2012), Global trends in tropical cyclone risk, *Nat. Clim. Change*, *2*(4), 289–294, doi:10.1038/nclimate1410.

Price, J. F. (1981), Upper ocean response to a hurricane, *J. Phys. Oceanogr.*, *11*(2), 153–175, doi:10.1175/1520-0485(1981)011<0153:UORTAH>2.0.CO;2.

Roarty, H. et al. (2010), Operation and Application of a Regional High-Frequency Radar Network in the Mid-Atlantic Bight, *Mar. Technol. Soc. J.*, *44*(6), 133–145, doi:10.4031/MTSJ.44.6.5.

Ruiz, S., L. Renault, B. Garau, and J. Tintoré (2012), Underwater glider observations and modeling of an abrupt mixing event in the upper ocean, *Geophys. Res. Lett.*, *39*, L01603, doi:10.1029/2011GL050078.

Sampson, C. R., and A. J. Schrader (2000), The automated tropical cyclone forecasting system (version 3.2), *Bull. Am. Meteorol. Soc.*, *81*(6), 1231–1240, doi:10.1175/1520-0477(2000)081<1231:TATCFS>2.3.CO;2.

Schofield, O., et al. (2007), Slocum gliders: Robust and ready, *J. F. Robot.*, *24*(6), 473–485, doi:10.1002/rob.20200.

Schofield, O., R. J. Chant, B. Cahill, and R. Castelao (2008), The decadal view of the Mid-Atlantic Bight from the COOLroom: Is our coastal system changing?, *Oceanography*, *21*(4), 108–117.

Seroka, G. N., T. N. Miles, Y. Xu, J. T. Kohut, O. Schofield, and S. M. Glenn (2016), Hurricane Irene sensitivity to stratified coastal ocean cooling, *Mon. Weather Rev.*, *144*(9), 3507–3530, doi:10.1175/MWR-D-15-0452.1.

Sherman, J., R. E. Davis, W. B. Owens, and J. Valdes (2001), The autonomous underwater glider "spray," *IEEE J. Oceanic Eng.*, *26*(4), 437–446.

Sopko, S. P., and R. J. Falvey (2014), Annual tropical cyclone report 2014: Joint Typhoon Warning Center, Joint Typhoon Warning Center, Pearl Harbor, Hawaii.

Tallapragada, V., C. Kieu, Y. Kwon, S. Trahan, Q. Liu, Z. Zhang, and I.-H. Kwon (2014), Evaluation of storm structure from the operational HWRF during 2012 implementation, *Mon. Weather Rev.*, *142*(11), 4308–4325, doi:10.1175/MWR-D-13-00010.1.

Torn, R. D., and C. Snyder (2012), Uncertainty of tropical cyclone best-track information, *Weather Forecast.*, *27*(3), 715–729, doi:10.1175/WAF-D-11-00085.1.

Umlauf, L., and H. Burchard (2003), A generic length-scale equation for geophysical turbulence models, *J. Mar. Res.*, *61*(2), 235–265, doi:10.1357/002224003322005087.

Warner, J. C., C. R. Sherwood, H. G. Arango, and R. P. Signell (2005), Performance of four turbulence closure models implemented using a generic length scale method, *Ocean Modell.*, *8*(1–2), 81–113, doi:10.1016/j.ocemod.2003.12.003.

Warner, J. C., W. C. Schwab, J. H. List, I. Safak, M. Liste, and W. Baldwin (2017), Inner-shelf ocean dynamics and sea floor morphologic changes during Hurricane Sandy, *Cont. Shelf Res.*, *138*(2017), 1–18, doi:10.1016/j.csr.2017.02.003.

Wilkin, J. L., and E. J. Hunter (2013), An assessment of the skill of real-time models of Mid-Atlantic Bight continental shelf circulation, *J. Geophys. Res. Oceans*, *118*, 2919–2933, doi:10.1002/jgrc.20223.

Zambon, J. B., R. He, and J. C. Warner (2014), Tropical to extratropical: Marine environmental changes associated with Superstorm Sandy prior to its landfall, *Geophys. Res. Lett.*, *41*, 8935–8943, doi:10.1002/2014GL061357.

Zhang, H., D. Chen, L. Zhou, X. Liu, T. Ding, and B. Zhou (2016), Upper ocean response to typhoon Kalmaegi (2014), *J. Geophys. Res. Oceans*, *121*, 6520–6535, doi:10.1002/2016JC012064.

Zhang, W. G., and G. G. Gawarkiewicz (2015), Dynamics of the direct intrusion of Gulf Stream ring water onto the Mid-Atlantic Bight shelf, *Geophys. Res. Lett.*, *42*, 7687–7695, doi:10.1002/2015GL065530.